Malvinas current at 44.7°S: First assessment of velocity temporal variability from in situ data

Guillermina Fernanda Paniagua, Martin Saraceno, Alberto R. Piola, Marcela Charo, Ramiro Ferrari, Camila Artana, Christine Provost

Progress in Oceanography

Malvinas Current at 44.7ºS: First assessment of velocity temporal variability from in situ data

--Manuscript Draft--

Manuscript Number:	
Article Type:	Full Length Article
Section/Category:	Physical and Geophysical Oceanography
Keywords:	MALVINAS CURRENT VARIABILITY; IN SITU TIME SERIES; ALTIMETRY DATA; PATAGONIAN SLOPE
Corresponding Author:	Guillermina Fernanda Paniagua, PhD Student CIMA: Centro de Investigaciones del Mar y la Atmosfera ARGENTINA
First Author:	Guillermina Fernanda Paniagua, PhD Student
Order of Authors:	Guillermina Fernanda Paniagua, PhD Student
	Martin Saraceno
	Alberto R. Piola
	Marcela Charo
	Ramiro Ferrari
	Camila Artana
	Christine Provost
Abstract:	Abstract We report current meter measurements obtained by four moorings deployed across the Malvinas Current (MC) at 44.7ºS during 18 months between December 2015-June 2017. Previous measurements of the MC strength have been reported only close to the Brazil-Malvinas Confluence, hindering the interpretation of the flow variability. The record-length time averaged velocities and variance ellipses indicate a strong northward along-isobath flow with an equivalent-barotropic structure. The meridional velocities at the western and eastern moorings are not correlated and show large amplitude oscillations which are coherent with the passage of mesoscale features over the moorings. Satellite altimetry data, that are highly correlated with 20-day low-pass filtered in situ velocities (r~0.80), show that the MC variability is affected by the propagation of sea level anomalies (SLA) along the Patagonian slope with phase speeds that range between 0.21 ± 0.04 m s -1 and 0.14 ± 0.01 m s -1 . SLAs propagate northward along the slope following contours of constant potential vorticity and its phase speeds decrease towards the east across the slope. SLAs that mostly affect the western mooring originate in the northern flank of the North Scotia Ridge while SLAs that mostly affect the eastern mooring originate along the Malvinas Escarpment, along the northern edge of the Malvinas Plateau. We suggest that the interaction between eddies and the complex bathymetry at those locations generate instabilities that enhance the generation of mesoscale structures that propagate in the flow direction along the western boundary of the Argentine Basin affecting the variability of the MC velocities.
Suggested Reviewers:	Magdalena Carranza magdalena@mbari.org
	Antonio Fetter antonio.fetter@ufpe.br
	Matthieu Le Hénaff m.lehenaff@miami.edu
Opposed Reviewers:	

Malvinas Current at 44.7ºS: First assessment of velocity temporal variability from in situ data

Guillermina F. Paniagua[1,2,3], Martin Saraceno[1,2,3], Alberto R. Piola[2,3,5], Marcela Charo[5], Ramiro Ferrari[1,2,3], Camila Artana[6] and Christine Provost[4]

[1] Centro de Investigaciones del Mar y la Atmósfera (CIMA/CONICET-UBA), Ciudad Autónoma de Buenos Aires, Argentina

[2] Departamento de Ciencias de la Atmósfera y los Océanos, Facultad de Ciencias Exactas y Naturales, Universidad de Buenos Aires, Buenos Aires, Argentina

[3] Unidad Mixta Internacional-Instituto Franco-Argentino para el Estudio del Clima y sus Impactos (UMI-IFAECI/CNRS-CONICET-UBA), Buenos Aires, Argentina

[4] Laboratoire d'Océanographie et du Climat: Experimentation et Approches Numériques (LOCEAN), UMR 7159, Paris, Francia

[5] Departamento de Oceanografía, Servicio de Hidrografía Naval (SHN), Buenos Aires, Argentina

[6] MERCATOR OCEAN, Parc Technologique du Canal, Ramonville Saint Agne, France

Corresponding author: Guillermina F. Paniagua (guillermina.paniagua@cima.fcen.uba.ar)

Highlights:

- Up to 18-months of in situ current data were obtained at 44.7°S at different depths within the Malvinas Current.
- The easternmost and westernmost meridional velocities are not correlated due to the presence of mesoscale features in the Malvinas Current.
- A large oscillation with a periodicity of about 40 days is observed in the meridional velocity measurements.

Abstract

We report current meter measurements obtained by four moorings deployed across the Malvinas Current (MC) at 44.7ºS during 18 months between December 2015-June 2017. Previous measurements of the MC strength have been reported only close to the Brazil-Malvinas Confluence, hindering the interpretation of the flow variability. The record-length time averaged velocities and variance ellipses indicate a strong northward along-isobath flow with an equivalent-barotropic structure. The meridional velocities at the western and eastern moorings are not correlated and show large amplitude oscillations which are coherent with the passage of mesoscale features over the moorings. Satellite altimetry data, that are highly correlated with 20-day low-pass filtered in situ velocities (r~0.80), show that the MC variability is affected by the propagation of sea level anomalies (SLA) along the Patagonian slope with phase speeds that range between 0.21 ± 0.04 m s^{-1} and 0.14 ± 0.01 m s^{-1}. SLAs propagate northward along the slope following contours of constant potential vorticity and its phase speeds decrease towards the east across the slope. SLAs that mostly affect the western mooring originate in the northern flank of the North Scotia Ridge while SLAs that mostly affect the eastern mooring originate along the Malvinas Escarpment, along the northern edge of the Malvinas Plateau. We suggest that the interaction between eddies and the complex bathymetry at those locations generate instabilities that enhance the generation of mesoscale structures that propagate in the flow direction along the western boundary of the Argentine Basin affecting the variability of the MC velocities.

Keywords

- MALVINAS CURRENT VARIABILITY
- IN SITU TIME SERIES
- ALTIMETRY DATA
- PATAGONIAN SLOPE

1. Introduction

The Malvinas Current (MC) originates as a branch of the Antarctic Circumpolar Current (Peterson and Whitworth, 1989; Piola and Gordon, 1989) veering northward approximately following the path of the Subantarctic Front into the western Argentine Basin. Reaching 38ºS, the MC causes the northernmost penetration of subpolar waters in the southern hemisphere. Thus, it contributes to the meridional heat transport and to regulate the climate on Earth (Garzoli and Matano, 2011). In situ current measurements have been collected mostly at 40-41ºS (Vivier and Provost, 1999a; 1999b; Spadone and Provost, 2009; Ferrari et al., 2017; Paniagua et al., 2018). At that latitude, the core of the current is observed above the 1000 m isobath (Vivier and Provost, 1999b; Spadone and Provost, 2009) and its flow might suffer large deflections for several months caused by the southward excursions of the Brazil Current (Paniagua et al., 2018). Indeed, the encounter between the MC and the southward flowing Brazil Current makes difficult to quantify the MC variability at 40-41ºS (Ferrari et al., 2017).

Further south, the first direct observations of surface currents over the shelf break were registered at 45ºS by hull-mounted downward-looking ADCP observations in late December 1992 (Saunders and King, 1995). The ADCP meridional velocity component in the 30-390 m depth interval presents an energetic northward flow spanning nearly 150 km (Saunders and King, 1995). Valla and Piola (2015) analyzed 52-days of direct current observations in 2005 from a downward-looking ADCP moored close to the upper portion of the shelf break at 43.8ºS and showed that the mean flow is strongly steered by the bottom topography. The combined analysis of surface drifters, satellite-derived geostrophic velocity and the ADCP data from Saunders and King (1995) showed that the MC flow at 45ºS is mainly concentrated in two narrow jets located just onshore of the 200 m and over the 1400 m isobaths (Piola et al., 2013). Surface velocities within the jets exceed 0.5 m s^{-1}. These jets extend more than 900 km from 47.5ºS to 39ºS along the Patagonian shelf break (Piola et al., 2013). Moreover, recent analyses of repeated hull-mount ADCP observations indicate that these two high-velocity jets are observed along the entire MC path from the northern Drake Passage to the Brazil/Malvinas Confluence (Frey et al., submitted). Numerical simulations partially agree with this observation: Fetter and Matano (2008) and Combes and Matano (2014) reported the presence of two jets extending from 55ºS and merge at approximately 45ºS.

The surface thermal structure between 39º and 44ºS and along the western limb of the MC is characterized by multiple fronts (Franco et al., 2008). Piola et al. (2013) pointed out the association between the time-averaged SST fronts and high-velocity jets of the MC. They showed that the location of the two across-shelf SST gradient minima, described for the first time by Franco et al. (2008), coincide with the two maxima satellite-derived meridional velocities that they found at 45ºS. These latter findings motivate a recent study that confirm, using deterministic and probabilistic tools from nonlinear dynamics, the expectation that the MC behaves as a barrier for cross-stream transport (Beron-Vera et al., 2020). Consequently, south of 38ºS, the MC promotes low connectivity between shelf waters and open-ocean waters off the shelf (Beron-Vera et al., 2020).

Furthermore, high chlorophyll-a concentrations observed during the austral spring and summer over the shelf break (Romero et al., 2006; Saraceno et al., 2005) suggest that the nutrient-rich subantarctic waters advected by the MC contributes to the large phytoplankton biomass observed along the shelf break (Acha et al., 2004; Romero et al., 2006). Indeed, the high productivity found in the shelf break front (Garcia et al., 2008; Lutz et al., 2010) is the main ecological feature that supports the production of tangible (fisheries) and intangible (recreation, regulation of atmospheric gases) marine ecosystems services (Martinetto et al., 2020). In particular, physical process along the shelf break sustain one of the most important fisheries of scallops in the southern hemisphere (Franco et al., 2017).

Several mechanisms have been proposed to explain the physical mechanism that sustain the primary productivity over a continental slope: enhanced mixing through tidal interaction with the continental slope (Rattray, 1960), the interleaving of water masses at the shelf break front (Fournier et al., 1979), the interaction between shelf-edge wave propagating northward along the slope and bottom topography (Dickson et al., 1980; Acha et al., 2004; Saraceno et al., 2005), the interaction of internal waves at the shelf break and wind-induced mixing (Maze et al., 1986), small-scale eddies propagating along the edge of the Malvinas Current (Podestá et al., 1990), horizontal divergence of the surface velocity field generated by the effect of bottom friction on the MC along the Patagonian shelf break (Matano and Palma, 2008; Combes and Matano, 2014) and wind-induced upwelling (Carranza et al., 2017). Yet, to the best of our knowledge, direct observations that may help elucidate which mechanisms contribute most to sustain the primary productivity observed, have not been reported.

The main objective of this work is to characterize the MC velocities through the analysis of the in situ measurements collected at 44.7ºS between December 2015 and June 2017. Improving the knowledge of MC dynamics is the first step to better understand the process that sustain the rich Patagonian shelf break ecosystem in future studies. In situ data analyzed on this work were obtained in the framework of the French-Argentine CASSIS project (www.cima.fcen.uba.ar/malvinascurrent). During 2015-2017, an array of nine mooring was deployed over a zonal section at 44.7°S across the continental shelf and shelf break (Figure 1a). In this study we focus on the analyses of the shelf break moorings. In section 2, we describe the data and methods used. In Section 3 we first present the results obtained through a statistical analysis of all in situ currents. We then focus on the possible mechanisms that cause the observed variability by combining the in situ velocity observations with satellite altimetry data. Sections 4 presents a discussion of the results and section 5 summarizes the conclusions.

2. Data and Methods

2.1. In situ Data

Nine current meter moorings were deployed in a zonal section, spanning the wide continental shelf and slope of the western margin of the Argentine Basin at 44.7ºS (Figure 1). Four moorings were deployed in the continental shelf and five over the shelf break and upper continental slope, perpendicularrly to the main direction of the isobaths (Figure 1a), from 1 December 2015 to 9 June 2017. In this study we examined the current meter data obtained across the continental slope (Figure 1b; Table 1). These moorings were deployed between the 200 and 2600 m isobaths (Figure 1; Table 1). From shallow to deep waters, the array consisted of a surface oceanographic buoy, one upward looking Acoustic Doppler Current Profiler (ADCP) and three tall-moorings referred to as M1, M2 and M3 (Figure 1). The oceanographic buoy was moored at 200 m depth and was equipped with a hull-mounted downward-looking Nortek Continental 190 kHz ADCP with an accuracy of 1% of the measured value and a resolution of 0.1 cm s^{-1}. The buoy was detached form its mooring 22 days after deployment. The upward looking ADCP was deployed at 1000 m depth but could not be recovered. The three tall-moorings were deployed over the 1320 m, 1945 m and

2608 m isobaths and comprised eleven Nortek Aquadopp current meters deployed at different depth (Figure 2). The measurement accuracy of Aquadopp current meters is 1% of the measured value ± 0.5 cm s^{-1}. M1 and M2 were deployed on November 26, 2015 and the oceanographic buoy and M3 between 13 and 16 May 2016. Hereinafter, instruments installed in the tall-moorings are labelled Mij where i represents the mooring number and j stands for the position within the mooring from the upper to the deepest instrument (Figure 2). Current meters moored on the tall-moorings M1 and M2 recorded data every half hour. Current meters on M3 recorded hourly data. Different sampling frequencies were adopted to optimize the number of samples, battery consumption, and memory capacity of each instrument as well as the aimed duration of the experiment.

The three tall-moorings were recovered between 8 and 10 June 2017. All current meters on M1 produced 528 to 554 days of high-quality data. Current meters on M3 recorded data for 390 days. Occasionally, the tall-moorings suffered large vertical displacements of up to 120 m that lasted as much as a few days. These events coincide with the largest MC intensities recorded. One month after deployment, M2 was accidentally lifted by a fishing vessel, dragged and released about 5 km east from the original location. As a result, the depth of the final position of M2 was 600 m deeper. Hereinafter we denote $M2_a$ the first 1 month-period of measurements (December 2015) and $M2_b$ the second and longest observation period (January 6, 2016 to June 9, 2017) (Figure 2). Table 2 summarizes data availability and basic statistics measured by the current meters. All data used in this work are available in Saraceno et al. (2020).

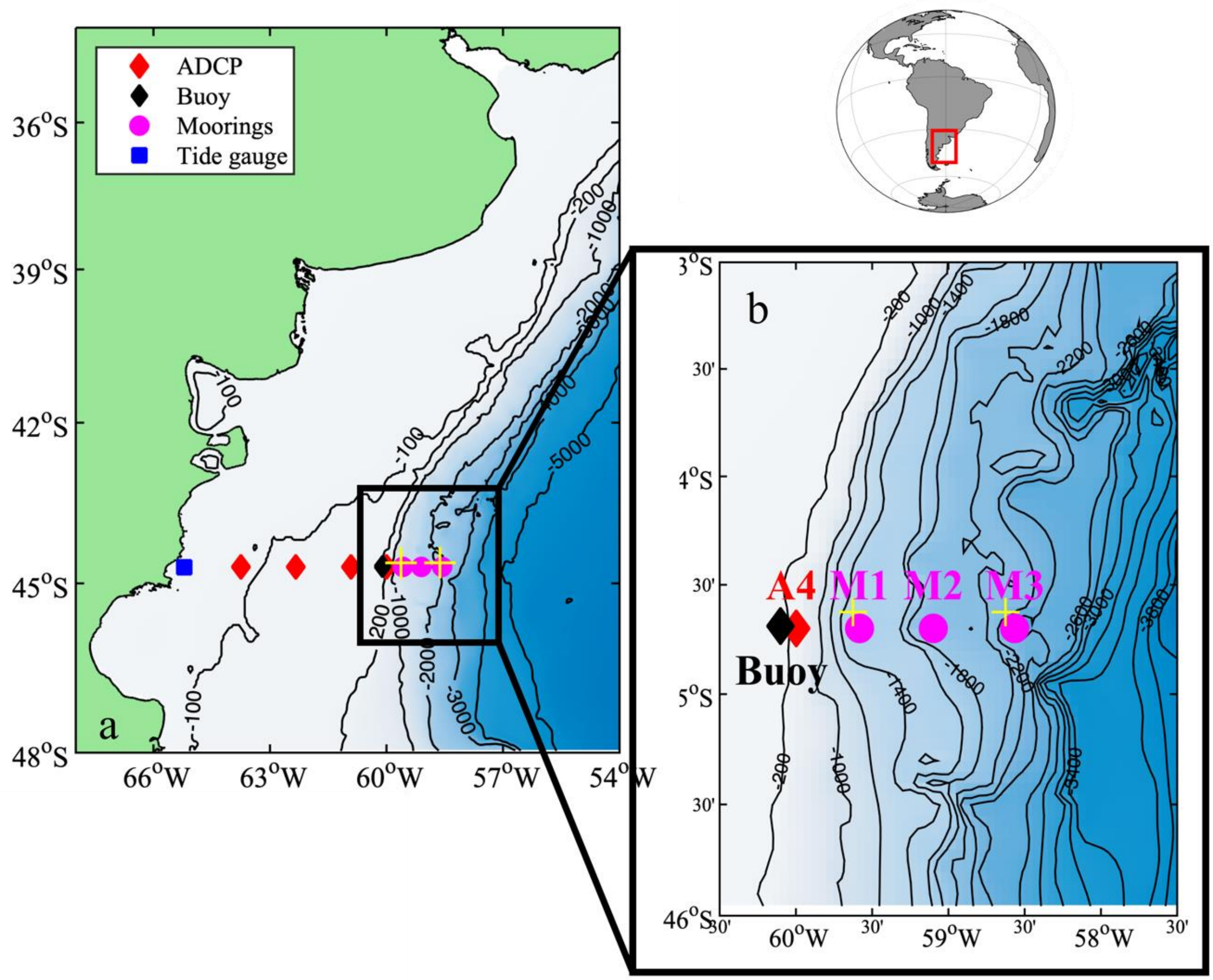

Figure 1. (a) Study region, moorings position and bathymetry. Color symbols represent the location of the moorings of the CASSIS project. The 100, 200, 1000, 2000 and 4000 m isobaths are indicated in black (GEBCO, (IOC, 2003)). (b) Enlarged map showing the location of the mooring array deployed in the shelf break from December 2015 to June 2017. The oceanographic buoy, the upward-looking ADCPs and the three tall-moorings are indicated with black and red diamonds and magenta circles respectively. The yellow crosses indicate the location from which the altimetry data were extracted to compare in-situ and satellite altimetry data.

2.2. Satellite Data

To examine the regional mesoscale field we used maps of absolute dynamic topography (MADT) derived from satellite altimetry and associated geostrophic velocities. Both altimeter products were downloaded from the Copernicus Marine Environment Monitoring Service (CMEMS, http://marine.copernicus.eu) site for the period 1993-2017. MADT and geostrophic velocities maps have a daily frequency and a horizontal resolution of 0.25x0.25 degree in a cartesian regular grid. Geostrophic velocity derived from satellite altimetry can be derived from gridded data constructed from multiple missions or from along-track mono-mission data. Gridded data compare better with in situ data than along-track data (Ferrari et al., 2012; Ferrari et al 2017). The agreement between in situ and satellite-derived velocities increases when a 20-day low-pass filter is applied to the in situ data (Ferrari et al., 2017).

2.3. Methods

All meridional (v) and zonal (u) velocity components were low-pass filtered with a cut-off period of 48 hours to remove tidal and inertial variability. Statistical parameters including mean and standard deviation of all low-pass filtered variables are given in Table 2 and Table 3. Spectra, confidence limits (CL) and significant peaks of the time series are calculated using the singular spectrum analysis multitaper method toolkit (Ghil et al., 2002). Two data tapers are used, and significant peaks have been estimated with the hypothesis of a harmonic process drawn back in a background red noise.

3 Results

3.1. Variability of the MC from in situ data

3.1.1. Velocity time series

All raw and 48h-low-pass filtered meridional and zonal velocities time series are displayed in the supplementary material (Figures S1-S9). A description of the low-pass filtered meridional and zonal velocities time series follows.

Oceanographic buoy

The meridional (along-isobath) velocity observed at the oceanographic buoy was always positive and reached maximum values of 68 cm s^{-1} at 20 m depth. The zonal velocity values at 20 m depth ranged between -13 cm s^{-1} (onshore) and 10 cm s^{-1} (Figure S1) suggesting significant cross-shelf break exchanges, though mean zonal (cross-shelf break) velocities are close to zero in the entire water column (see supporting information in Figure S1 and Table 3). Similar charactersistics were reported by Valla and Piola (2015) based on a 52-day current meter time series at approximately the same location.

M1

The meridional velocity component observed at M1 was positive most of the time at all depths (Figure 3a and supporting information Figures S2a, S3a and S4a). No meridional reversals were observed in the shallowest instrument moored at 300 m depth (M11) and only one flow reversal event was recorded at 760 m depth (M12) in July 2016, and on six occasions at 1042 m depth (M13). The flow reversals lasted between one and seven days. As in the shelf edge, the meridional velocity was much larger than the zonal velocity, reaching maximum values of 61.4 cm s^{-1} at M11 (300 m, Figures 3a and supporting information Figure S2a). In addition, all records at M1 present large oscillations (up to 50 cm s^{-1}) in the meridional velocity at all depths (Figure 3a). As will be shown later, these oscillations appear to be generated by mesoscale structures that interact with the the bathymetry further south. On the other hand, the zonal components of the currents at M1 show values ranging between -22 cm s^{-1} and 24 cm s^{-1} with mean values close to zero in the entire water column (Figure 3c, supporting information Figures S2b, S3b and S4b and Table 2).

M2

Meridional velocities at $M2_a$ were always northward (positive) down to 1315 m depth. Only two flow reversals were recorded at 1720 m depth, the deepest current meter deployed at $M2_a$ (Figures S5a, S6a and S7a). The zonal velocity values at $M2_a$ fluctuated between -17 cm s^{-1} and 26 cm s^{-1} and the mean zonal velocity was close to zero, as observed at M1 (Figure S5b, S6b and S7b; Table 2).

After M2 was displaced eastward, the whole mooring dropped 600 m, so all observationes were recorded between 1560 and 2270 m depth. At $M2_b$ we observed a different behavior compared to

$M2_a$. The meridional velocity component observed at $M22_b$ (1560 m) and $M23_b$ (1865 m) were positive most of the time, while at $M24_b$ (2270 m), the meridional velocity fluctuated around zero as well as the zonal velocities observed at all depths at this location (Figures S5a, A6a and S7a). An interesting observation is that the amplitude of the oscillations at $M22_b$, $M23_b$ and $M24_b$ of the zonal currents increases with depth (Figure S5b, S6b and S7b).

M3

At M3, the easternmost tall-mooring, current velocity was measured at four levels ranging from 500 to 2100 m depth (Figure 2). As observed at M1 and $M2_a$, the meridional velocities were positive almost of the time except in a few occasions when current reversals were observed. During the time period analyzed here, the instruments recorded a minimum of one to a maximum of fourteen meridional flow reversals and the number of reversals increased downward (Figure 3e and supporting information Figures S8a, S8c, S9a and S9c). Furthermore, large oscillations were present in the meridional velocity at all depths as observed at M1. The average zonal velocity of the four current meters is not significantly different from zero (Table 2). The amplitude of the oscillations of the zonal velocities recorded at M3 are much larger than those observed at M1 (Figure 3g and supporting information Figures S8b, S8d, S9b and S9d).

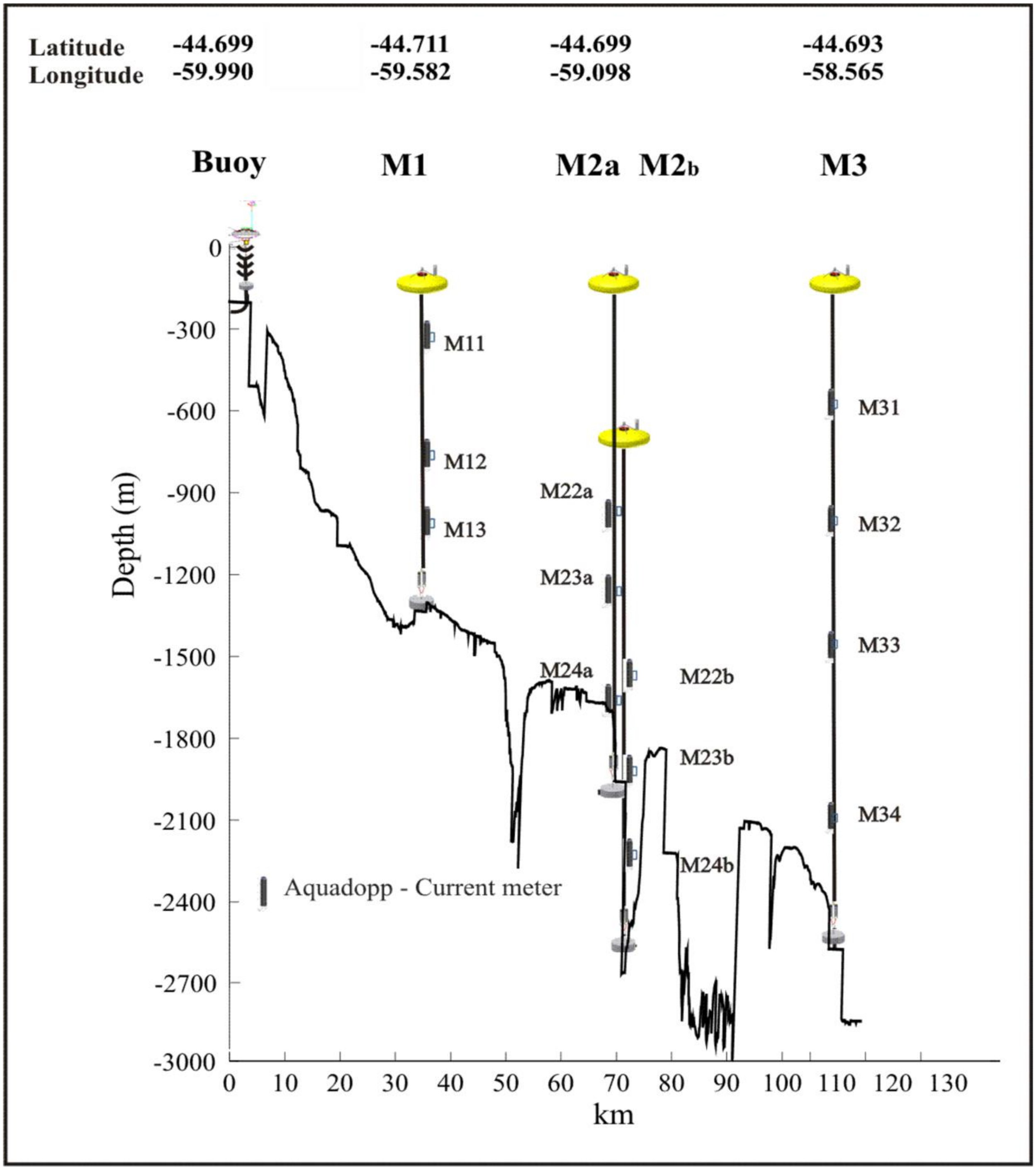

Figure 2. Location and vertical distribution of the current meters deployed along 44.7ºS between December 2015 and June 2017. The oceanographic buoy was the only mooring with a surface buoy that transmitted data on real-time. It was deployed at 200 m depth. The bathymetry displayed was reconstructed with echo-sounder data obtained during the deployment cruises.

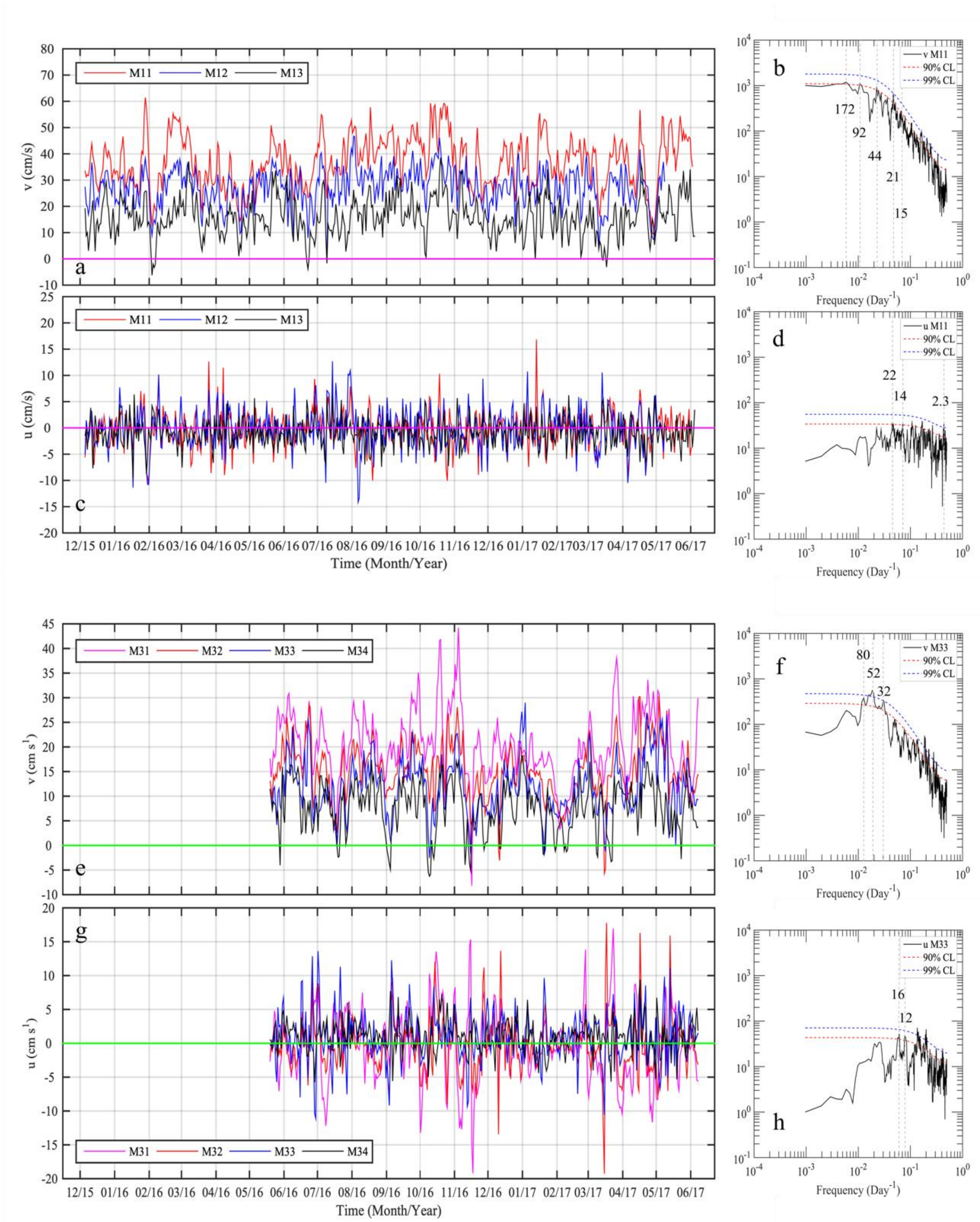

Figure 3. In situ time series of meridional and zonal velocities observed at M1 (a, c) and M3 (e, g). Color lines correspond to 48 h low-pass filtered daily data. Horizontal magenta and green lines

indicate the zero value. Spectra ((cm/s)^2/cpd) of meridional and zonal currents at (b, d) 300 m (M11) and at (f, h) 1486 m (M33). The red and blue dashed lines in all the right panels, indicate 90% and 95% confidence levels (CL), respectively. Also, the black vertical dashed lines and the associated numbers indicate significant periodicities in days. See Figure 2 for spatial location of the moorings.

3.1.2. Mean velocity and velocity variance ellipses

Time and depth average current velocities are 46.6, 27, 16, 5.1, and 13.8 cm s^{-1} at the oceanographic buoy, M1, M2$_a$, M2$_b$, and M3, respectively. The relatively low mean velocity observed at M2$_b$ is due to the fact that all observations are deeper than 1500 m. As the direction of the mean flow at M1, M2$_a$ and M3 is northward, we conclude that the mean flow at this latitude is strongly constrained by the local bathymetry (Figure 4). At all locations the mean velocities decrease with depth (Figure 4; Tables 2 and 3), suggesting an equivalent-barotropic structure as previously reported based on observations at 41°S (e.g. Vivier and Provost, 1999b). Through the entire water column, the time-averaged velocities observed at M1 are higher in comparison with the time-averaged velocities observed at the easternmost mooring: the mean values range between 37.3 cm s^{-1} at 300 m (M11) and 16.1 cm s^{-1} at 1042 m depth (M13) (Figure 4; Table 2). The large mean values observed at M1 suggest that the MC is stronger at this longitude, in good agreement with observations made from previous snap-shot observations at 45ºS (Saunders and King, 1995; Piola et al., 2013, Frey et al., 2020). The direction of the major axes of the variance ellipses is northward, indicating that the largest fluctuations occur in the same direction of the mean flow at all moorings and depths, except close to the bottom at M24$_a$ (1720 m) and at all depths at M2$_b$ (Figure 4). The distinct observations collected at M2$_b$ will be described separately below. The variability of the zonal component is higher at M3 compared with M1 (Figure 4) because M3 is more exposed to the intense mesoscale activity present in the open ocean (Figure 1). This observation is in agreement with previous reports of the variability of the zonal component of the MC at 41°S (e.g. Paniagua et al., 2018).

The direction of the mean flow and the variance ellipses at M2$_b$ (Figure 4) are quite different from those observed at M1 and M3. The mean flow direction in the upper two instruments (M22$_b$ and

$M23_b$ located at 1560 m and 1865 m depth) is towards the northeast, with means exceeding the standard deviations. The deepest instrument ($M24_b$ at 2270 m depth) shows a nearly zero velocity mean and a velocity variance ellipse oriented nearly perpendicular to the direction of the mean MC flow (Figure 4). The bathymetry was recorded by a Kongsberg EA600 12/600 kHz single beam hydrographic echo sounder on the R/V Puerto Deseado during the deployment cruise over the moorings (displayed in Figures 2 and 4). The mean velocity vectors and variance ellipses observed at $M23_b$ (1865 m) and $M24_b$ (2270 m) (Figure 4) suggests that these observations were collected within a a hole or a submarine canyon with a southwest-northeast orientation, i.e. parallel to the mean axis of variance the flow at $M24_b$. The latter results clearly suggests that the flow at $M24_b$ is strongly controlled by the local bathymetry. Submarine canyons are quite common in the region (Lastras et al., 2011), despite their location is not reported in the majority of seafloor maps. While the analysis of the flow into the submarine canyon is certainly very interesting, it is out of the scope of this work and will not be covered within this article.

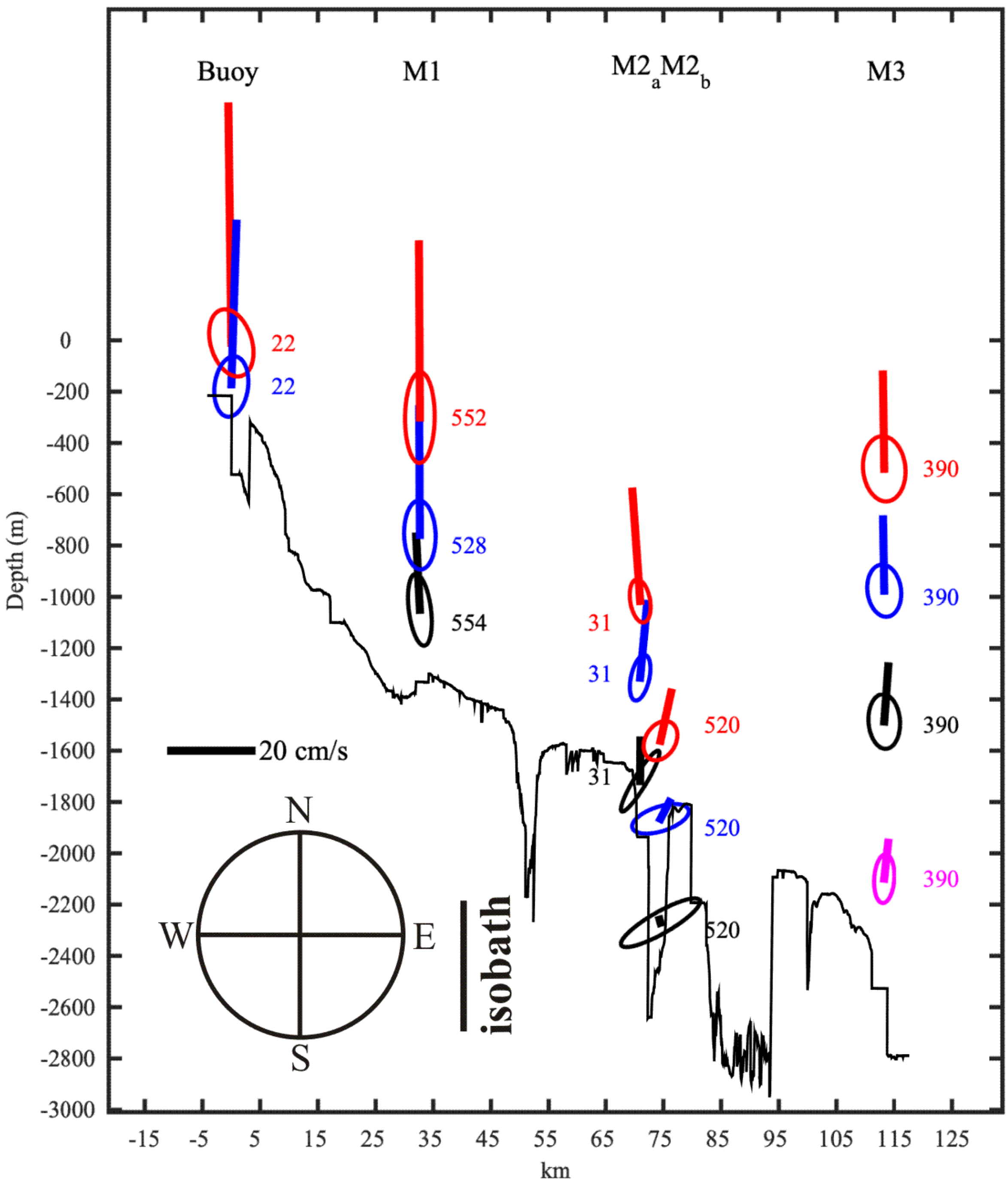

Figure 4. Mean flow and variance ellipses of the time series obtained by the current meters. The number of days that each instrument measured are indicated. The average orientation of the isobaths at 44.7ºS is indicated by the thick line at the bottom. The black line corresponds to the topography along the section where the moorings were deployed. The *X* axis is the distance along the section in km, the origin being the buoy location.

3.1.3. Spectral and vertical coherence analysis of the velocity time series measured on the MC

The meridional and zonal velocity time series observed at M1 and M3 show a vertically coherent flow (Figures 3a, 3c, 3e and 3g). To determine the scales that dominate the time variability of the flow we estimate the spectra of the meridional and zonal components of the current velocity registered at M1 and M3. The spectral analysis of all the meridional components measured at M1 and M3 show significant periodicities around 85, 40, 20 and 15 days (Figure 3). In addition, the spectral estimates of the zonal component at M1and M3 reveals significant peaks in a broad band of periodicities between 25 and 2 days (Figure 3). The spectra of the zonal velocity at M34 (2100 m) denoted significant periodicities centered at 55 days (not shown).

The vertical coherence between the meridional and the zonal velocity components at M1 shows, in most cases, that the two components are coherent at 52, 25, 18 and 13 days (Figures S10a and S10b). The coherence analysis carried out between the meridional and zonal velocities at M31 (500 m), M32 (976 m) and M33 (1486 m) denoted a significant vertical coherence at 38, 19, 13 and 8 days (Figures S10c and S10d). No significant coherence was observed between M34 and the shallower observations at that location. This suggests that the processes that induce the velocity variations at 2100 m depth, near the seabed, are uncoupled from those that modulate the velocity variability at shallower levels.

3.1.4. Principal modes of variability of the MC velocities

To further quantify the variability of the vertical structure of the MC, we computed empirical orthogonal functions (EOFs) of the time series collected at M1 and M2. The spatial patterns of the three leading modes and the time series associated with moorings M1 and M3 are displayed in Figure 5.

The first leading EOF (EOF1) of M1 and M3 explains 69% and 51% of the total variance, respectively (Figure 5a). The spatial patterns of EOF1 at M1 and at M3 (Figure 5a) and the high correlations between the time series of respective EOF1 and the meridional velocity at M11 (0.93, 95% CL) and M31 (0.86, 95% CL) (Figures 5b and 5d) clearly characterize this mode as an along-isobath mode of velocity fluctuations. The spatial pattern of EOF1 at M1 is surface-intensified and has a downward counter-clockwise rotation with depth while the spatial mode of EOF1 at M3 shows similar intensities in the vertical and a downward clockwise rotation (Figure 5a).

EOF3 of M1 and EOF2 of M3 explain 9% and 20% of the total variance, respectively (Figure 5a) and represent variations in the across-isobath velocity at M1 and M3. This is confirmed by the high correlations (0.78, 95% CL) between the associated time series of these modes and the zonal velocity component at the shallowest observed level at each location (Figure 5 c and e).

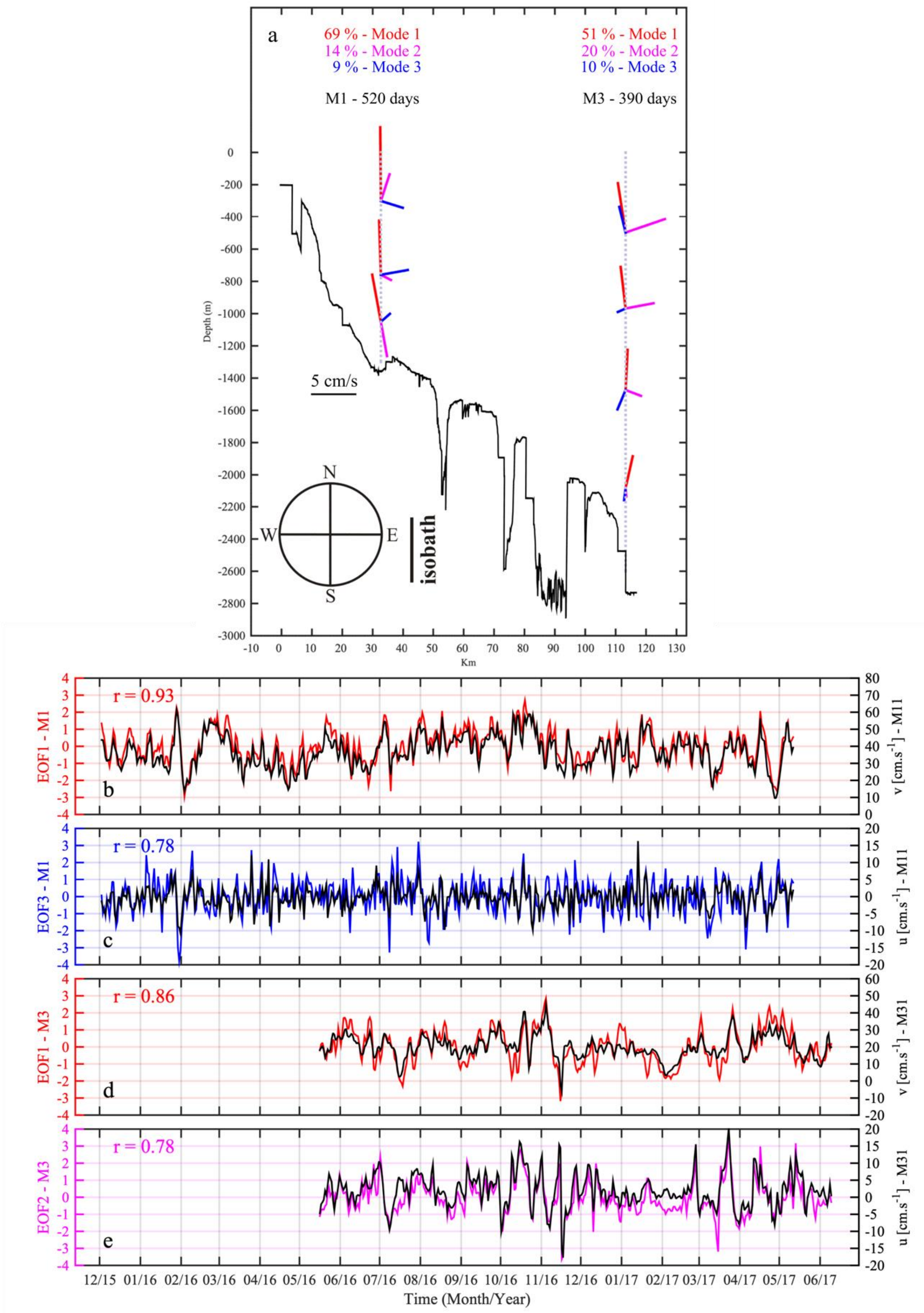
a
69 % - Mode 1
14 % - Mode 2
9 % - Mode 3
M1 - 520 days
51 % - Mode 1
20 % - Mode 2
10 % - Mode 3
M3 - 390 days
Depth (m)
5 cm/s
N
W
E
S
isobath
Km
EOF1 - M1
r = 0.93
b
v [cm.s-1] - M11
EOF3 - M1
r = 0.78
c
u [cm.s-1] - M11
EOF1 - M3
r = 0.86
d
v [cm.s-1] - M31
EOF2 - M3
r = 0.78
e
u [cm.s-1] - M31
12/15 01/16 02/16 03/16 04/16 05/16 06/16 07/16 08/16 09/16 10/16 11/16 12/16 01/17 02/17 03/17 04/17 05/17 06/17
Time (Month/Year)

Figure 5. (a) Spatial pattern of the empirical orthogonal functions (EOFs) of the velocity field of M1 and M3 tall-moorings; the percentage of total variance explained by mode 1, 2 and 3 of each EOF is denoted in red, magenta and blue, respectively. EOFs are computed separately for each mooring. The average orientation of the isobaths is indicated by the thick line at the bottom. Vertical scale in meters; horizontal scale in kilometres. (b) Time series of EOF1 at M1 (red) and meridional velocity (cm s^{-1}) at M11 (black). (c) Time series of EOF3 at M1 (blue) and zonal velocity (cm s^{-1}) at M11 (black). (d) Time series of EOF1 at M3 (red) and meridional velocity (cm s^{-1}) at M31 (black). (e) Time series of EOF2 at M3 (magenta) and zonal velocity (cm s^{-1}) at M31 (black). In the four bottom panels, the correlation between time series is indicated in the top left corner.

3.1.5. Spectral analysis of the EOFs time series

The spectra of EOF1 at M1 and M3, that characterize the along-isobath (meridional) velocity variations, show significant periodicities (Figure S11, a-b) similar to those described in section 3.1.4 in the spectral analysis performed for each meridional velocity time series measured at M1 and at M3, respectively (Figures 3b and 3f). In addition, EOF3 which characterizes the zonal velocity variability at M1showed significant peaks in the same frequency band (Figure S11c) as all the zonal velocity time series at M1 (Figure 3d). On the other hand, the spectra of EOF2 at M3 displays a significant periodicity centered at 25 days (Figure S11d). The 25-day peak was only significant in the spectral estimates of the zonal velocity component observed at M31 (300 m depth) and M32 (1070 m depth) (not shown).The wavelet power spectra of the EOFs time series indicates that those periodicities occur seldomly (Figures S12 and S13). This suggests that several processes force the observed oscillations and that those processes are not periodic in time. In the following section we show that the propagation of SLA are a likely contributor to this velocity variability pattern.

3.2. On the origin of the MC variability at 44.7ºS

In the following section we first compare the 20-day low pass in situ velocities with the geostrophic velocities computed from satellite gridded altimetry data closest to M1 and M3 locations. We then use satellite altimetry data to unveil the origin of the oscillations observed in the in situ velocity described in Section 3.1.

3.2.1. Comparison between in situ and satellite altimetry velocities

The 20-day low-pass filtered meridional and zonal velocities at 300 m depth at M1 are significantly correlated with the meridional and zonal velocities derived from gridded satellite altimetry data closest to the mooring location (0.74 and 0.55, respectively, Figures 6c and 7c). At M31 (500 m depth) the correlations of the meridional and zonal velocities with the altimetry derived velocities are higher: 0.80 and 0.85 , respectively (Figures 6a and 7a). Therefore, in agreement with previous studies (Ferrari et al., 2017) satellite altimetry appears to be a good proxy to monitor currents at periods longer than 20 days. However, some of the largest oscillations present in the low-pass filtered in situ velocities (e.g. oscillations of up to 50 cm s^{-1} in less than a week in the meridional velocities at M11 and at M31; grey line in Figures 6a and 6c) are not captured by altimetry data.

At M1 (M3), the mean meridional velocity obtained from altimetry between December 2015-June 2017 (May 2016-June 2017) is 7 (6) cm s^{-1} larger than the mean value of the meridional velocity component observed at the shallowest current meter moored at M11 (M31) around 300 m (500 m) depth (Tables 3 and 4). This result is expected since the MC flow has a barotropic-equivalent structure and, therefore, the magnitude of the velocity decreases with depth. On the other hand, the satellite-derived current velocities do not represent the most superficial currents of the ocean. Indeed, at the buoy, the comparison between satellite altimetry and in situ velocities recorded by the downward-looking ADCP at 10 m intervals in the whole water column, shows that the best match occurs at 120 m depth (Table 3).

3.2.2. Variability of the MC in time and space

Given the signficant correlation between satellite altimetry and in situ velocities, to better understand the variability observed at the mooring locations we used the MADT and derived geostrophic velocities to examine the two-dimensional surface flow field. In spite of the proximity between M1 and M3 (80 km), the correlation between the satellite-derived meridional velocities is non-significant (r = -0.05 and p-value = 0.26). Furthermore, the mean satellite-derived meridional component at M1 location is almost twice as large as that observed at M3 (Figure 6b;

Table 4). On the other hand, a significant, though low correlation is found between satellite-derived zonal velocities at M1 and M3 (r = 0.33 and p-value = 1 x 10^{-15}). In this case, the mean zonal velocity at M1 is four times larger than the mean value observed at M3 (Figure 7b; Table 4).

A longitude versus time diagram of satellite-derived meridional velocities across the mooring section during the study period (Figure 6b) suggests an explanation for the different variability patterns observed at M1 and M3. The temporal mean of the meridional velocity derived from satellite altimetry along the section between 62ºW and 57ºW suggest that the core of the MC (> 40 cm s^{-1}) lies very close (~20 km) to M1 (Figure 6b, left panel). In mid-April 2016, a sharp decrease in meridional velocities (from 45 cm s^{-1} to less than 30 cm s^{-1} based on the altimetry data) was observed throughout the entire section. On the other hand, from August to November 2016, the MC increased its intensity reaching a maximum of 62.5 cm s^{-1} in August. In late April 2017, the core of the MC moved closer to M3 (Figure 6b, right panel). This last event generated a large increase (decrease) in the meridional velocity over M3 (M1) (Figures 6a and 6c). In the following section we will discuss the possible origin of the variability observed in the meridional velocities at M1 and M3.

We also analyzed the longitude versus time diagram of the satellite-derived zonal velocities along the section at 44.7ºS and between 62 and 57ºW during the study period (Figure 7b). The time mean zonal velocity is highest (~4.5 cm s^{-1}) very close to the shelf break, suggesting a weak net offshore flow. This is the only portion of the section where the time mean is significantly different from zero. In addition, the cross-shore velocity standard deviation increases from the edge of the shelf break to the open ocean (Figure 7b, left panel). Between M1 and M3 the zonal velocities are low and are negative on several occasions (Figure 7b, right panel).

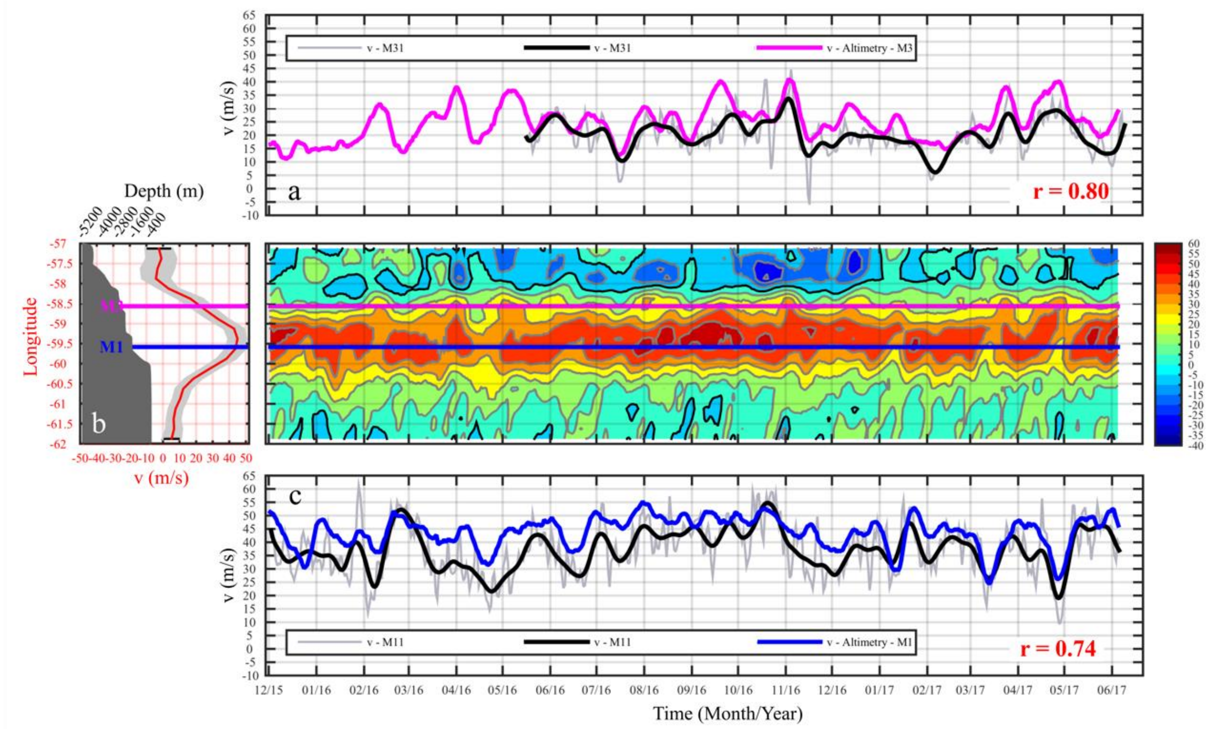

Figure 6. (a) In situ time series of the 2 and 20 days low-pass filtered daily resampled meridional velocity component at M31 are indicated with grey and black lines, respectively. The magenta line shows the time series of the meridional component of the surface velocity derived from satellite altimetry near M3. Correlation between the 20-day low pass filtered in situ time series and the altimeter time series is indicated in the bottom right corner. (b) Right panel: Longitude vs time plot of the meridional component of the current derived from satellite altimetry along 44.7ºS and between 62 and 57ºW. The blue (magenta) line represent the longitude of M1 (M3). Left panel: mean (red) and standard deviations (grey shading) of the meridional velocity derived from the altimeter. The topography along the section at 44.7ºS and between -62 and -57ºW is displayed in dark grey. (c) As panel (a) for the meridional velocity at M11 (grey and black lines) and altimetry at that location (blue).

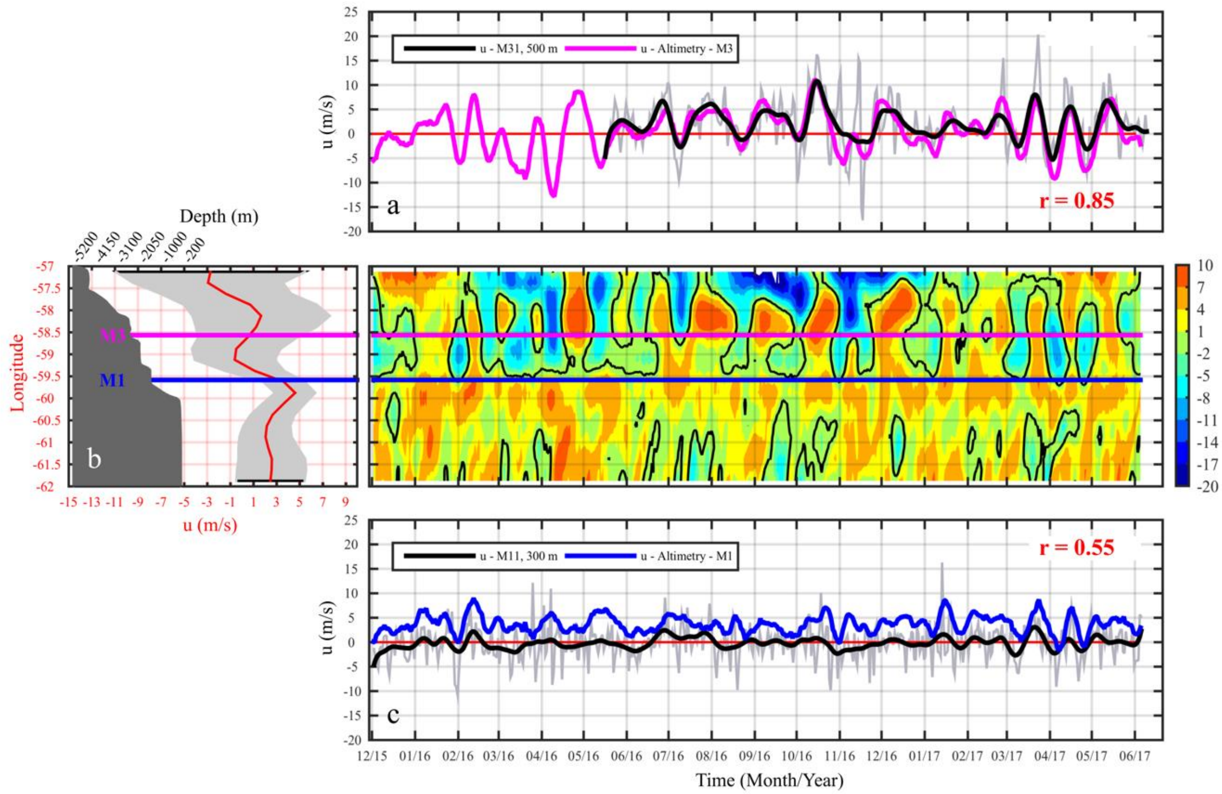

Figure 7. (a) In situ time series of the 2 and 20 days low-pass filtered daily resampled zonal velocity component at M31 are indicated with grey and black lines, respectively. The magenta line shows the time series of the zonal component of the surface velocity derived from satellite altimetry near M3. Correlation between the 20-day low pass filtered in situ time series and the altimeter time series is indicated in the bottom right corner. (b) Right panel: Longitude vs time plot of the meridional component of the current derived from satellite altimetry along 44.7ºS and between 62 and 57ºW. The blue (magenta) line represent the longitude of M1 (M3). Left panel: mean (red) and standard deviations (grey shading) of the zonal velocity derived from the altimeter. The topography along the section at 44.7ºS and between -62 and -57 ºW is displayed in dark grey. (c) As panel (a) for the zonal velocity at M11 (grey and black lines) and altimetry at that location (blue).

3.2.3. Relationship between the Malvinas Current and sea level anomaly

Sea level anomaly (SLA) maps show that mesoscale structures pass nearby or in-between the moorings and have a significant impact on the observed velocity variability. To illustrate this interaction, a sequence of SLA maps is displayed in Figure 8. On April 29, 2017 an anticyclonic eddy with an amplitude of 18.2 cm and 85 km mean radius is observed between M1 and M3 (Figure 8a). Hereinafter we refer to this eddy as Matias. The positive SLA at the eddy core induces anticyclonic circulation. The location of Matias on April 29, 2017, should decrease the strength of the equatorward flow at M1 and increase it at M3. This is in agreement with the meridional velocity variations derived from in situ observations (Figures 6a and 6c). To determine the origin of Matias we identified and followed the positive SLA in previous SLA maps (Figure 8b-h). This suggests that Matias was originated from two distinct positive SLA anomalies located near 53°W over the Malvinas Plateau in early February 2017 (Figure 8h). These features appear to merge in early March and subsequently displace westward and northward approximately following the isobath orientations and eventually reaching the mooring array in late April (Figure 8f-a). The latter observation suggests that a fraction of the along-isobath velocity variability is due to the downstream propagation of mesoscale features. To determine at which location along the moorings the SLA variations had the most significant impact, we computed the correlation between the SLA along 44.7ºS and the meridional velocity at M11 (300 m depth; Figure 9a) and at M31 (500 m depth; Figure 9b), respectively. Results shows that the variability of the MC observed at M11 and M31 is dominated by the SLA centered east of each mooring location. The highest correlation between SLA and the meridional velocity at M11 (M31) was found 30 (40) km east of the mooring location . In the following, we refer to the locations where we found the highest correlation between SLA and the meridional velocity at M11 and at M31 as locations A (44.7ºS; 59.1ºW) and B (44.7ºS; 57.9ºW), respectively (Figures 9a and 9b). Figure 9c (9d) shows the time series of the along-slope velocity observed at M11 (M31) and the SLA time series obtained at A (B) location. Figure 9a also suggests that the variability of the SLA over the shelf break (~60ºW) does not affect the meridional velocity at M1.

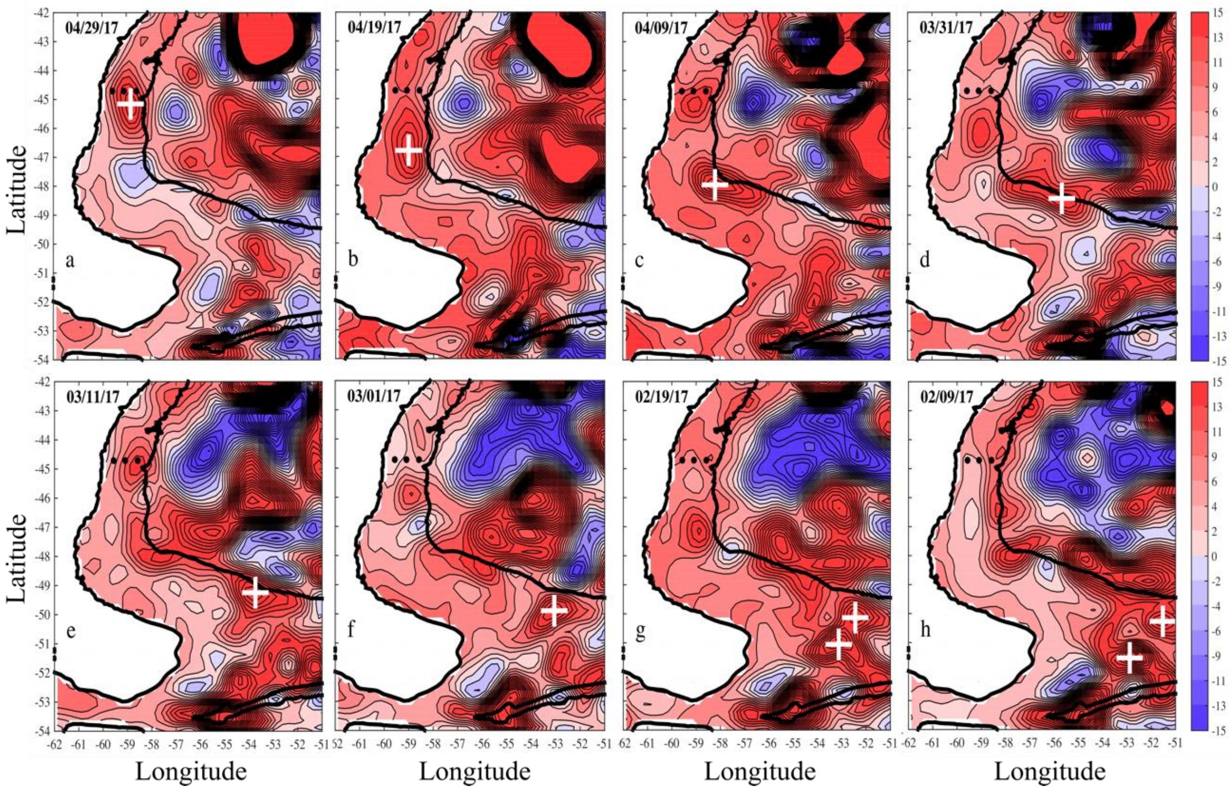

Figure 8. Distribution of sea level anomaly (SLA) between April 29, 2017 (a) and February 2, 2017 (h). Local maxima of positive SLA on the continental slope are indicated by a white cross. The 200 and 3000 m isobaths are indicated with black lines (GEBCO, (IOC, 2003)). The position of the moorings are indicated with black circles.

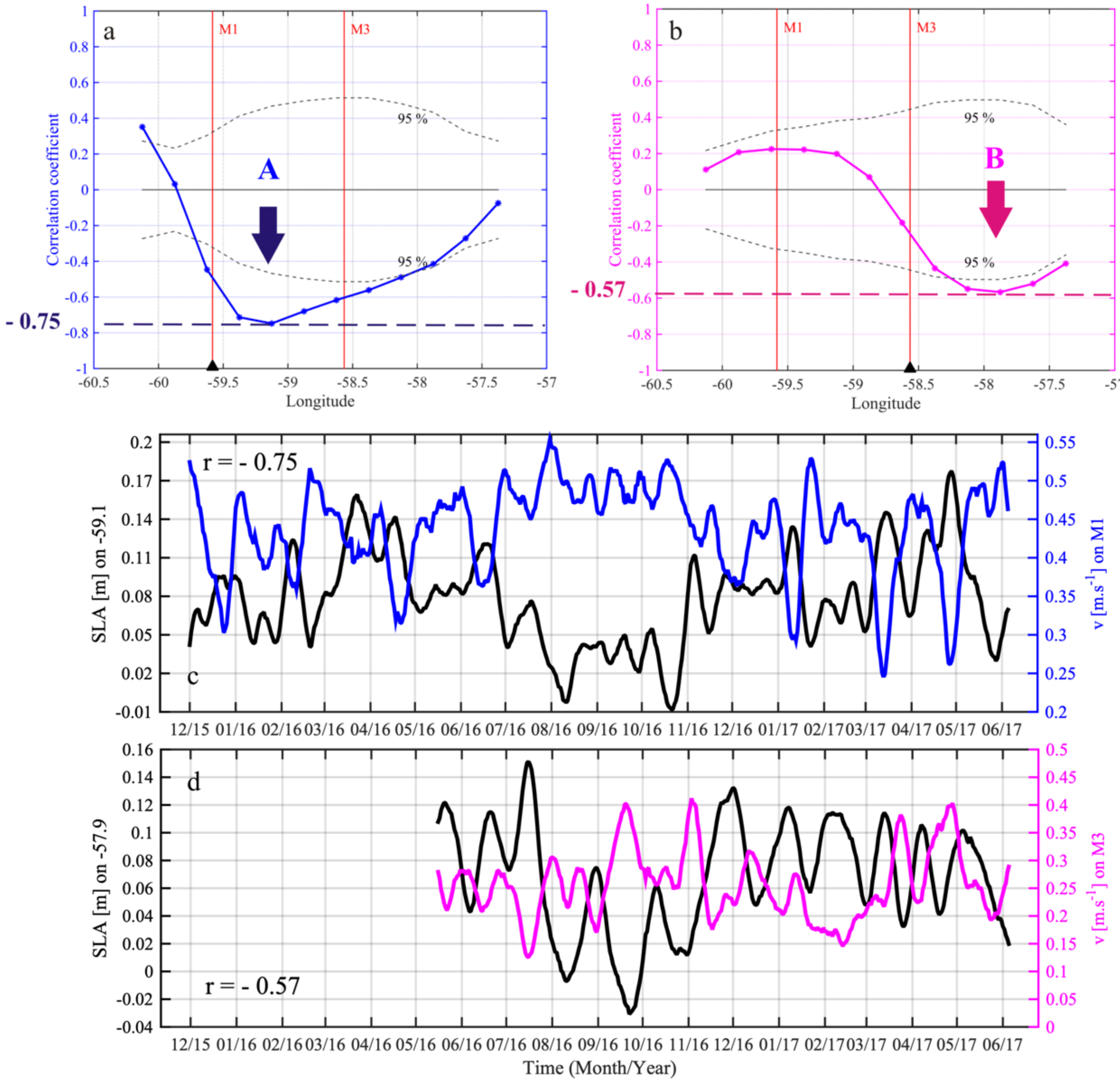

Figure 9. (a) Correlation between satellite-derived meridional velocity (***v***) close to M1 and SLA across the MC at 44.7ºS. The position of the moorings M1 and M3 are indicated by vertical red lines. The black dashed lines indicate 95% confidence levels. (b) As in panel (a) for M3. (c) Time series of satellite derived meridional velocity (***v***) close to M1 (blue) and SLA (black) at the location of maximum correlation observed in panel (a) (44.7ºS; 59.1ºW). (d) Time series of satellite derived meridional velocity (***v***) close to M3 (magenta) and SLA (black) at the location of maximum correlation observed in panel (b) (44.7ºS; 57.9ºW).

3.2.4. Propagation of SLA along the western slope of the Argentine Basin

In the previous section we showed that the variability of the MC observed at M1 and M3 at 44.7ºS is mostly affected by the SLA variability 30 km and 40 km east of the mooring locations respectively. Here, we show that the main contributor of the SLA variability observed at those locations (A and B) is due the presence of SLA that propagate northward through the array. Assuming that the MC flows mainly along constant planetary potential vorticity (PV) contours (e.g. Saraceno et al., 2004) we examined the SLA variability from December 2015 to June 2017 along the contours of constant PV that correspond to A and B locations (Figure 10). The PV contour selected is $-2.9x10^{-8}$ m^{-1} s^{-1} for A and $-5.2x10^{-8}$ m^{-1} s^{-1} for B locations. The PV contours selected correspond roughly to the 1950 m and 3500 m isobaths at 44.7ºS (Figure 10a). These PV contous run approximately parallel to each other along the western margin of the Argentine Basin, but sharply diverge south of 49°S, with the $-2.9x10^{-8}$ m^{-1} s^{-1} PV extending southward and westward and the $-5.2x10^{-8}$ m^{-1} s^{-1} PV running eastward along the northern flank of the Malvinas Plateau. The slanted pattern of SLA anomalies along these paths (Figure 10b and 10c) are indicative that those anomalies are propagating along the contours selected. So far the results show that the propagation of SLA along the selected PV contours contribute to the meridional velocity fluctuations observed at 44.7°S. We suggest that the SLA could be associated with the presence of mesoscale structures (or eddies) that propagate along the Patagonian slope.

Furthermore, Figures 10b and 10c show that the SLA arriving at 44.7ºS originates at different locations. Figure 10b shows that most of the SLA that propagate along the PV from W1 to W2 (Figure 10a) originate in the northern flank of the North Scotia Ridge, at about (53.5ºS, 56ºW) and, occasionally, at about 50ºS and 53ºW (Figures 10a and 10b). On the other hand, Figure 10c shows that the majority of the SLA that propagate along the PV from E1 to E2 can be tracked up to 49.6ºS and 47.2ºW and occasionally up to 49.3ºS and 39.6ºW, suggesting that the origin of these SLA is along the Malvinas Escarpment, in the northern flank of the Malvinas Plateau. After passing through the array, SLAs continue travelling northward along the slope until they dissipate about around 40ºS (Figure 10). The large amplitude of SLA observed north of 40ºS is indicative of the alternating impact of subtropical and subantarctic waters, characteristic of the encounter of the Brazil and Malvinas Currents at the Confluence. These larger amplitude SLA fluctuations may mask the northward propagation of SLA beyond the Confluence.

The mean phase speed propagation of the SLA was determined by the slope of slanted SLA pattern displayed in Figures 10b and 10c. From 50ºS to 40ºS, the SBTW that propagate along the PV contours from W1 to W2 are slightly faster (mean phase speeds = 0.17 ± 0.02 m s^{-1}) than those that propagate along the PV from E1 to E2 (mean phase speeds = 0.14 ± 0.01 m s^{-1}). We also observed that the SLA that propagate between W1 and E1 taked ~2.5 months to reach the location of the moorings from 50ºS, (Figure 10). A similar time took Matias to reach 44.7ºS from 50ºS (Figures 8a-f).

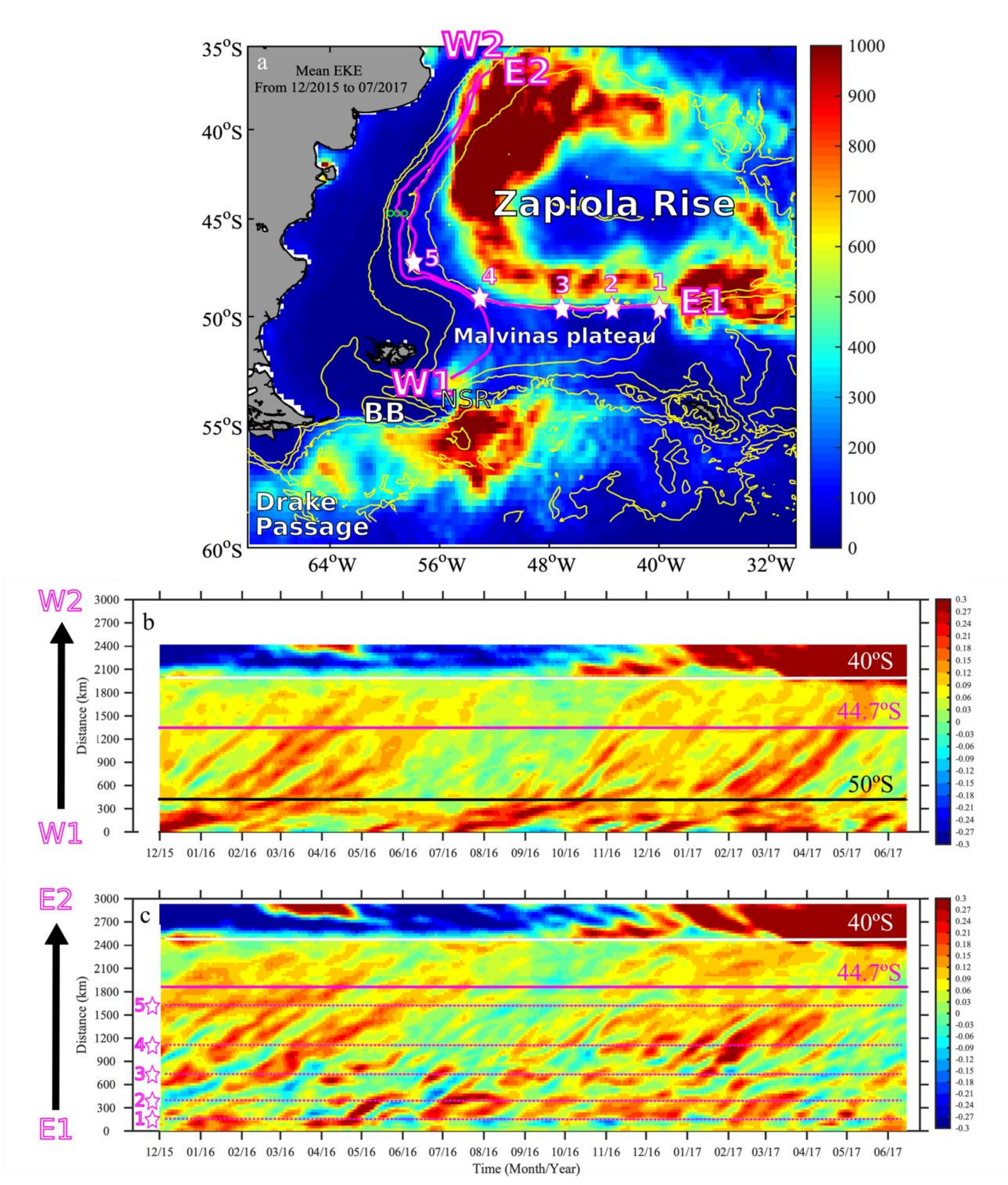

Figure 10. (a) Mean eddy kinetic energy (EKE) ($cm^2\ s^{-2}$) derived from satellite-derived SLA between December 2015 and July 2017. Yellow contours indicate the 200, 1000, 3000 and 5000 m isobaths (GEBCO, (IOC, 2003)). The location of the North Scotia Ridge, Drake Passage, Malvinas Plateau, Zapiola Rise and Burdwood Bank (BB) are indicated. Magenta lines correspond

to contours of constant potential vorticity (PV) that passed over the maxima correlation points indicated in Figure 9. The five white stars located on the PV from E1 to E2 indicate distances from E1. From the 1st to the 5th star, the distances from E1 are: 110, 400, 690, 1100 and 1580 m. The green circles indicate the location of the moorings. (b) Distance vs time plot of SLA along the constant PV line from W1 to W2 indicated in panel (a). The magenta line indicates the latitude of the mooring's location. The y-axis shows the distance from south to north (in km). (c) As in (b) but for the constant potential vorticity line from E1 to E2 in panel (a). The five magenta dashed lines denote the distances from "E1" indicated by stars in panel (a).

To further explore the SLA along the western slope of the Argentine Basin, we tracked the SLA variability along five additional PV contours that correspond to the 550, 1100, 1400, 2450 and 2750 m isobaths at 44.7ºS (Figure S14 and S15 a-g). Results show that there are SLA that propagate northward along all the selected PV contours and that their phase speeds decrease in the offshore direction from 0.21 ± 0.04 m s^{-1} to 0.14 ± 0.01 m s^{-1} (Figure S15 b-g). On the other hand, the vertical lines observed in the Hovmöller diagram of the SLA along the PV contour of -20 10^{-8} m^{-1} s^{-1} (500 m isobath at 47ºS, Figure S15a) are associated with the propagation of fast SLA which are only observed along the upper portion of the slope. The propagation speed of these fast SLA cannot be resolved with the available altimetry data.

Finally, taking advantage of the availability of the satellite altimetry data, we extended the analysis of the SLA along the PV contours from 1993 to 2017. We find a pattern similar to the one obtained during the December 2015 - July 2017 period: SLA propagating northward along the slope (Figure S16). A spectral analysis of the 24 years SLA time series extracted at A and B locations (Figures 9a and 9b) show significant peaks at a near-annual time scale and between 25 and 140 days at both locations (Figure 11).

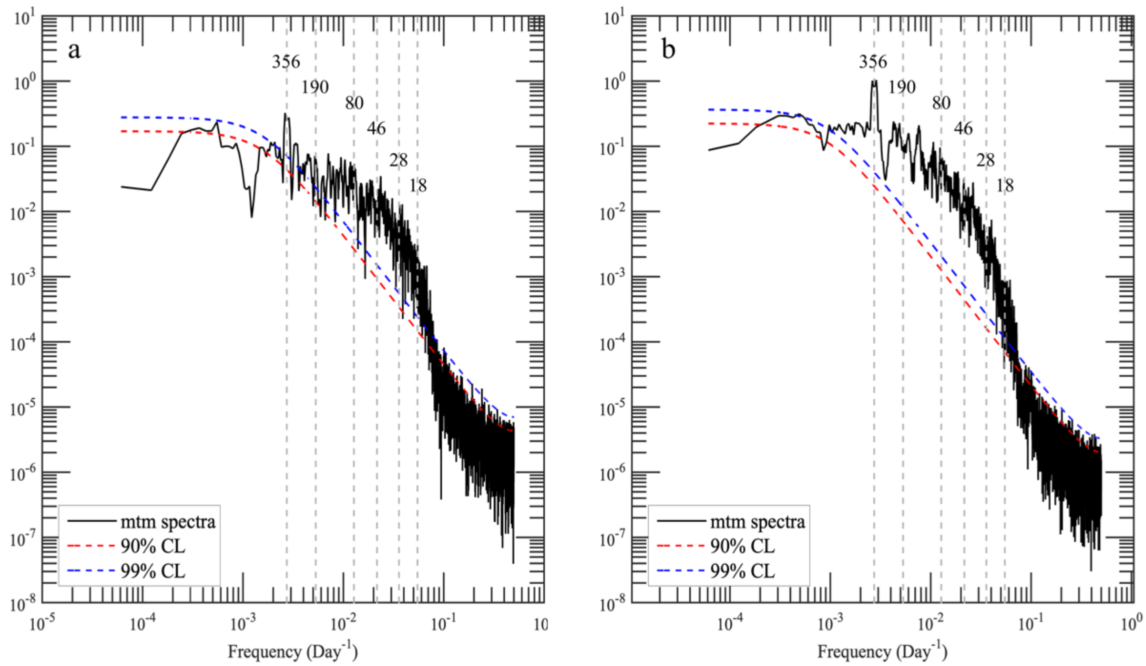

Figure 11. Spectra (m^2/cpd) of the SLA time series at the intersection of 44.7ºS with the constant PV = -5.2 10^{-8} m^{-1} s^{-1} (a) and PV = -2.9 10^{-8} m^{-1} s^{-1} (b). Vertical dashed lines and numbers indicate significant periodicities in days.

4 Discussion

The MC has been studied from observations during the past 30 years around 41ºS. At that latitude, the proximity of the Brazil-Malvinas Confluence severely impacts the time variability of the MC (Ferrari et al., 2017). The observations described here, collected at 44.7ºS, provide the first evaluation of the MC variability away from the complexity introduced by the Confluence.

Mean velocities at M1, $M2_a$ and M3 suggest that the MC has an equivalent-barotropic structure and flows parallel to the isobaths along the continental shelf break at 44.7ºS, in good agreement with previous estimates based on hydrographic (Piola and Gordon, 1989) and current meter observations further north (Vivier and Provost, 1999a; Ferrari et al., 2017; Paniagua et al., 2018). In a few occasions, the equatorward surface velocities of the MC decreased up to a 30% relative to their time averaged means (Figure 6c). The largest decreases in meridional velocity occur when eddies interact with the MC, strongly modifying the velocity structure of the MC. Similar events were reported by Artana et al., (2016) at these latitudes.

The analysis of the SLA revealed (i) that the MC variability at M1 and M3 locations is partially due to the presence of SLAs that propagate northward along the continental slope and (ii) the regions from where the SLAs originate. From West to East, the phase speed of the SLA decrease from 0.21 ± 0.04 m s^{-1} to 0.14 ± 0.01 m s^{-1}. A decrease in phase speed can be associated with a decrease in the bottom slope (Gill, 1982). In our region it is difficult to estimate the bottom slope, given the complexity of the bathymetry (Figure 2). Yet, without considering the small canyons it is right to assume that the bottom slope decreases eastwards and therefore provides a possible explanation for the decrease in the phase speed observed according to Gill (1982 . Fu (2006), used the generic term "eddies" to represent the various forms of mesoscale SLAs and estimated similar phase speeds (~0.12 m s^{-1}) for the propagation of eddies along the Patagonian slope between 50ºS to 45ºS. Our results sugges that the passage of such SLAs affect the MC meridional velocities at 44.7ºS. The propagation of SLAs that we are observing are much slower than the coastally trapped waves that have been reported along the Patagonian shelf break and that have been associated with Kelvin waves propagating from the equatorial Pacific (Clarke and Ahmed, 1999; Vivier et al., 2001; Cravatte et al., 2003; Artana et al., 2016; Combes and Matano, 2019).

We showed that the MC is affected by SLA, such eddies and filaments, that propagate along the continental slope. The interaction between western boundary currents and propagating mesoscales features has been documentes also in other places. For example, in the North Atlantic, the variability of the deep western boundary current (DWBC) is also affected by meanders and eddies (Biló and John, 2020) that are probably generated by westward propagating Rossby wave-like perturbations (Meinen and Garzoli, 2014; Biló and John's, 2020).

A significant 25-day periodicity is revealed by the spectra of the zonal velocity at M3 (EOF2 of M3, Figure S11d). Based on the the analysis of SLA variability, Fu et al. (2001) reportered the existence of topographic Rossby waves with a period close to 25 days that propagate around the Zapiola Rise, a sedimentary elevation about 1200 m in height, centered at 43ºW-45ºS (Figure 10a). Fu (2007) provided further evidence of the interaction between the large 25-day waves and the energetic mesoscale variability in the Argentine basin. These observations suggest that the 25-day peak that characterizes the zonal currents at M3 may be due to the barotropic topographic Rossby waves described by Fu et al. (2001) that reach the east side of the MC, close to M3 location (Figure 10a).

SLA variations that modulate the intensity of the MC at 44.7°S can be tracked upstream to the northern flank of the North Scotia Ridge at about 53.5ºS and 56ºW and to the northern flank of the Malvinas Plateau, along the Malvinas Escarpment (Figure 10). These regions coincide with local maxima of eddy kinetic energy in the Southwestern Atlantic (Figure 10a). Several studies suggest that these regions of large eddy kinetic energy are associated with the interaction of the flow with the complex bottom topography (Fu, 2006; Fetter and Matano, 2008; Saraceno and Provost, 2012; Artana et al., 2016; Mason et al., 2017). Our analyses suggest that these regions are likely sources of SLAs that propagate in forms of mesoscale structures (or eddies) along the Patagonian slope and modulate the strength of the MC. The estimated propagation velocity and origin of the SLAs derived in this study are in agreement with recent analyses of a numerical model (Poli et al., 2020).

5 Summary of conclusions

18-months of in situ current observations over the western slope of the Argentine Basin at 44.7ºS show mean northward velocities up to 37 ± 9.7 cm s^{-1} at 300 m depth. The in situ meridional velocities observed 80 km apart are not correlated due the presence of mesoscale features within the Malvinas Current. The flow is vertically coherent up to 1500 m depth both in M1 and M3. The 20-day low pass filtered in situ and satellite-derived meridional velocities are significantly correlated (~0.8), suggesting that the latter is a good proxy to monitor currents variations at time scales longer than 20 days. The variations in the intensity of the Malvinas Current at 44.7ºS are modulated by variations in sea-level anomaly that originate in the northern flank of the North Scotia Ridge (53.5ºS, 56ºW) and along the Malvinas Escarpment (~50ºS, 47.2-39.6ºW). The anomalies propagate northward closely following lines of constant potential vorticity. The SLA reaching the onshore flank of the Malvinas Current along the upper slope originate mostly from the northern flank of the North Scotia Ridge, while those arriving at the offshore flank originate along the northern edge of the Malvinas Plateau near 40ºW. The SLA that propagate along the offshore flank are slower than those that propagate along the onshore flank of the MC.

Acknowledgments, Samples, and Data

A large number of people helped collecting the in situ data that are the core of the results presented here. The cruises were performed with the collaboration of the offshore rescue vessel SB-15 Tango (Prefetcura Naval Argentina) and R/V Puerto Deseado (Consejo Nacional de Investigaciones Científicas y Tecnológicas). The cruises carried out with the offshore rescue vessel SB-15 Tango and the R/V Puerto Deseado were financed by Prefetcura Naval Argentina and Servicio de Hidrografía Naval, respectively. We particularly thank the support of the following institutions: SHN, Mincyt, INIDEP, CONICET, UBA, Prefectura Naval Argentina, Puerto Deseado crew, CNRS, Sorbonne Université LOCEAN, LOPS and DT-INSU. This study is a contribution to EUMETSAT/CNES DSP/OT/07-2118 and DSP/OT/07-4571, CONICET-FYPF PIO 133-20130100242. Additional support was provided by grant CRN3070 from the Inter-American Institute for Global Change Research through NSF grant GEO-1128040. GFP benefited from doctoral scholarship from CONICET, Argentina. Satellite data are available at Copernicus Marine Environment monitoring service (CMEMS) (http://marine.copernicus.eu/). In situ data are available at SEANOE (www.seanoe.org cf reference below Saraceno et al., 2020).

767 **References**

768 Acha, E. M., H. W. Mianzan, R. A. Guerrero, M. Favero, and J. Bava (2004), Marine fronts at
769 the continental shelves of austral South America - Physical and ecological processes, *J.*
770 *Mar. Syst.*, *44*, 83–105.
771 Artana, C., R. Ferrari, Z. Koenig, M. Saraceno, A. R. Piola, and C. Provost (2016). Malvinas
772 Current variability from Argo floats and satellite altimetry, *J. Geophys. Res. Oceans*, *121*,
773 4854– 4872, doi:10.1002/2016JC011889
774 Beron-Vera, F. J., Bodnariuk, N., Saraceno, M., Olascoaga, M. J., and Simionato, C. (2020).
775 Stability of the Malvinas Current. *Chaos: An Interdisciplinary Journal of Nonlinear*
776 *Science*, *30*(1), 013152.
777 Biló, T. C. and Johns, W. E. (2020). The Deep Western Boundary Current and Adjacent Interior
778 Circulation at 24°–30°N: Mean Structure and Mesoscale Variability. *Journal of Physical*
779 *Oceanography*, *50*(9), 2735-2758.
780 Carranza, M. M., Gille, S. T., Piola, A. R., Charo, M., and Romero, S. I. (2017). Wind
781 modulation of upwelling at the shelf-break front off Patagonia: Observational evidence, *J.*
782 *Geophys. Res. Oceans*, *122*, 2401–2421, doi:10.1002/2016JC012059
783 Clarke, A. J., and Ahmed, R. (1999). Dynamics of remotely forced intraseasonal oscillations off
784 the western coast of South America. *J. Phys. Oceanogr.*, *29*, 240–258.
785 Cravatte, S., Picaut, J., Eldin, G., (2003). Second and first baroclinic kelvin modes in the
786 equatorial pacific intraseasonal timescales. *J. Geophys. Res. 108 (C8*), 3266, http:
787 //dx.doi.org/10.1029/20 02JC0 01511
788 Combes, V., and Matano, R. P. (2014). A two- way nested simulation of the oceanic circulation
789 in the Southwestern Atlantic. *Journal of Geophysical Research: Oceans*, *119*(2), 731-756.
790 https://doi.org/ 10.1002/2013JC009498
791 Combes, V., and Matano, R. P. (2019). On the origins of the low-frequency sea surface height
792 variability of the Patagonia shelf region. *Ocean Modelling*, *142*, 101454.
793 Dickson. R. R., Gurbutt, P. A., and, Pillai, V. N. (1980). Satellite evidence of enhanced
794 upwelling along the European continental slope. *J. Phys. Oceanogr. 10*, 813-819.
795 Ferrari, R., Provost, C., Renault, A., Sennéchael, N., Barré, N., Park, Y. H., and Lee, J. H.
796 (2012). Circulation in Drake Passage revisited using new current time series and satellite
797 altimetry: 1. The Yaghan Basin. *Journal of Geophysical Research: Oceans*, *117*(C12).

Ferrari, R., Artana, C., Saraceno, M., Piola, A. R., and Provost, C. (2017). Satellite altimetry and current-meter velocities in the Malvinas Current at 418S: Comparisons and modes of variations. *Journal of Geophysical Research: Oceans*, *122*, 9572–9590. https://doi.org/10.1002/ 2017JC013340

Fetter, A. F. H., and Matano, R. P. (2008). On the origins of the variability of the Malvinas Current in a global, eddy-permitting numerical simulation, *J. Geophys. Res.*, *113*, C11018, doi:10.1029/2008JC004875

Fournier. R. O., van Det, M., Wilson, J. S., and Hargreaves, N. B. (1979). Influence of the shelf-break front off Nova Scotia on phytoplankton standing stock in winter. *J. Fish. Res. Board Can. 36,* 1228-1237.

Franco, B. C., Piola, A. R., Rivas, A. L., Baldoni, A., and Pisoni, J. P. (2008). Multiple thermal fronts near the Patagonian shelf break, *Geophys. Res. Lett.*, *35*, L02607, doi:10.1029/2007GL032066.

Franco, B. C., Palma, E. D., Combes, V., and Lasta, M. L. (2017). Physical processes controlling passive larval transport at the Patagonian Shelf Break Front. *Journal of Sea Research*, *124*, 17-25.

Frey, D. I., Piola, A. R., Krechik, V. A., Fofanov, D. V., Morozov, E. G., Silvestrova, K. P., Tarakanov, R. Y., and Gladyshev, S. V. (2020). Direct measurements of the Malvinas Current velocity structure, submitted to *J. Geophys. Res. Oceans*.

Fu, L.-L., Cheng, B., and Qiu, B. (2001). 25-day period large-scale oscillations in the Argentine Basin revealed by the TOPEX/Poseidon altimeter. *J. Phys. Oceanogr.*, *31***,** 506–517.

Fu, L.-L. (2006). Pathways of eddies in the South Atlantic Ocean revealed from satellite altimeter observations. *Geophys. Res. Lett., 33*, L14610, doi:10.1029/2006GL026245

Fu, L.-L., (2007). Interaction of mesoscale variability with large-scale waves in the Argentine Basin. *J. Phys. Oceanogr., 37*, 787 – 793, doi:10.1175/ JPO29911

Garzoli, S. L., and Matano, R. (2011). The South Atlantic and the Atlantic meridional overturning circulation. *Deep-Sea Research Part II, 58*(17), 1837-1847.

Ghil, M., Allen, R. M., Dettinger, M. D., Ide, K., Kondrashov, D., Mann, M. E., Robertson A., Saunders, A., Tian, I., Varadi, F., and Yiou, P. (2002). Advanced spectral methods for climatic time series. *Reviews of geophysics*, *40*(1), 3-1.

Gill, A. E. (1982). The Tropics, In William L. Donn (Ed.), *Atmosphere-Ocean dynamics* (Vol. 30, pp. 429-457). San Diego, International Geophysics Series.

IOC, IHO, and BODC (2003). ‘‘Centenary Edition of the GEBCO Digital Atlas’’, published on CD-ROM on behalf of the Intergovernmental Oceanographic Commission and the International Hydrographic Organization as part of the General Bathymetric Chart of the Oceans; British Oceanographic Data Centre, Liverpool.

Lastras, G., Acosta, J., Muñoz, A., and Canals, M. (2011). Submarine canyon formation and evolution in the Argentine Continental Margin between 44°30’S and 48°S. *Geomorphology, 128,* 116–136, doi:10.1016/j.geomorph.2010.12.027.

Lutz, V. A., Segura, V., Dogliotti, A. I., Gagliardini, D. A., Bianchi, A. A., and Balestrini, C. F. (2010). Primary production in the Argentine Sea during spring estimated by field and satellite models. *Journal of Plankton Research*, *32*(2), 181-195.

Martinetto, P., Alemany, D., Botto, F. *et al.* (2020). Linking the scientific knowledge on marine frontal systems with ecosystem services. *Ambio* (49), 541–556. https://doi.org/10.1007/s13280-019-01222-w

Mason, E., Pascual, A., Gaube, P., Ruiz, S., Pelegrí, J. L., and Delepoulle A. (2017). Subregional characterization ofmesoscale eddies across the Brazil-Malvinas Confluence. *J. Geophys. Res.Oceans*, *122*, 3329–3357, doi:10.1002/2016JC012611

Matano, R. P., and Palma, E. D. (2008). On the upwelling of downwelling currents. *Journal of Physical Oceanography*, 38, 2482–2500. https:// doi.org/10.1175/2008JPO3783.1

Mazé, R., Camus, Y., and Le Tareau, J. Y. (1986). Formation de gradients thermiques à la surface de l'océan, au-dessus d'un talus, par interaction entre les ondes internes et le mélange dû au vent. *ICES Journal of Marine Science, 42*(3), 221-240.

Meinen, C. S., and Garzoli, S. L. (2014). Attribution of deep western boundary current variability at 26.5ºN. Deep-Sea Res., 90, 81–90, https://doi.org/10.1016/j.dsr.2014.04.016.

Paniagua, G. F., Saraceno, M., Piola, A. R., Guerrero, R., Provost, C., Ferrari, R., et al. (2018). Malvinas Current at 40ºS–41ºS: First assessment of temperature and salinity temporal variability. Journal of Geophysical Research: Oceans, 123. https://doi.org/ 10.1029/2017JC013666.

Peterson, R.G., and Whitworth III, T. (1989). The Subantarctic and Polar Fronts in relation to deep water masses through the southwestern Atlantic. *Journal of Geophysical Research: Oceans*, *94*(C8), 10817-10838.

Peterson, R. G., and Stramma, L. (1991). Upper-level circulation in the South Atlantic Ocean. *Progress in oceanography*, *26*(1), 1-73.

Piola, A. R., and Gordon, A. L. (1989). Intermediate Waters in the Southwest South-Atlantic, *Deep-Sea Res., Part I, 36*(1), 1–16, doi:10.1016/ 0198-0149(89)90015-0.

Piola, A. R., Franco, B. C., Palma, E. D., and Saraceno, M. (2013). Multiple jets in the Malvinas Current, *J. Geophys. Res. Oceans, 118*, 2107–2117, doi:10.1002/jgrc.20170.

Podesta, G. P. (1990). Migratory pattern of Argentine hake Merluccius hubbsi and oceanic processes in the Southwestern Atlantic Ocean. *Fishery Bulletin*, *88*(1), pp.167-177.

Poli, L., Artana, C., Provost, C., Sirven, J., Sennéchael, N., Cuypers, Y., and Lellouche, J. M. (2020). Anatomy of subinertial waves along the Patagonian shelf break in a 1/12° global operational model. *Journal of Geophysical Research: Oceans*, e2020JC016549.

Rattray, M. (1960). On the coastal generation of internal tides. *Tellus, 12*, 54-62.

Romero, S. I., A. R. Piola, M. Charo, and C. A. E. Garcia (2006), Chlorophyll-a variability off Patagonia based on SeaWiFS data, *J. Geophys. Res.*, *111*, C05021, doi:10.1029/2005JC003244.

Saraceno, M., Provost, C., Piola, A. R., Bava, J., and Gagliardini, A. (2004). Brazil Malvinas Frontal System as seen from 9 years of advanced very high resolution radiometer data, *J. Geophys. Res., 109*, C05027, doi:10.1029/2003JC002127.

Saraceno, M., Provost, C., and Piola A. R. (2005). On the relationship between satellite-retrieved surface temperature fronts and chlorophyll a in the western South Atlantic, *J. Geophys. Res.*, *110*(C11), C11016, doi:10.1029/2004JC002736.

Saraceno, M., and Provost, C. (2012). On eddy polarity distribution in the southwestern Atlantic. *Deep Sea Research Part I: Oceanographic Research Papers*, *69, 62-69.*

Saunders, P. M., and King, B. A. (1995). Bottom currents derived from a shipborne ADCP on WOCE cruise A11 in the South Atlantic, *Journal of Geophysical Research*, *25*(3), 329–347.

Saraceno, M., Provost C., Piola, A., Guerrero, R., Ferrari, R., Paniagua G. F., Lago, L. S. and Artana, C. (2020). Malvinas Current 2015-2017: Mooring velocities. SEANOE. https://doi.org/10.17882/76617.

Spadone, A., and Provost, C. (2009). Variations in the Malvinas Current volume transport since October 1992. *Journal of Geophysical Research, 114*, C02002. https://doi.org/10.1029/2008JC004882

Valla, D., and Piola, A. R. (2015), Evidence of upwelling events at the northern Patagonian shelf break, *J. Geophys. Res. Oceans*, *120*, doi:10.1002/2015JC011002

Vivier, F., and C. Provost (1999a), Direct velocity measurements in the Malvinas Current, *J. Geophys. Res.*, *104*, 21083–21104.

Vivier, F., and Provost, C. (1999b). Volume transport of the Malvinas Current: Can the flow be monitored by TOPEX/POSEIDON? *Journal of Geophysical Research*, 104, 21,105–21,122.

Vivier, F., Provost, C., and Meredith, M. (2001). Remote and local forcing in the Brazil Malvinas Region, *J. Phys. Oceanogr.*, *31*, 892–913, doi: 10.1175/1520-0485.

Tables

Table 1. Mooring Locations.

Mooring name	Latitude (ºS)	Longitude (ºW)	Bottom depth (m)	Deployment date	Recovery date
Buoy	-44.7	-59.9	200	5/16/2016	6/7/2016
M1	-44.7	-59.6	1320	11/26/2015	6/8/2017
M2	-44.7	-59.1	1945	11/26/2016	6/9/2017
M3	-44.7	-58.6	2608	5/14/2016	6/10/2017

Table 2. Statistics of current meters measurements over the continental Patagonian shelf break between December 2015 and June 2017. M*ij* denotes current meters at moorings M1, M2, and M3, *i* being the mooring number and *j* standing for the level from the surface (see Figure 2). Here, **ϴ** is the angle in degrees of mean velocity direction relative to the geographical north, **V** (cm s^{-1}) is the magnitude of the time-average velocity and v (cm s^{-1}) and u (cm s^{-1}) are the velocity components, σ is the standard deviation and unless otherwise specified, mean values are indicated. All statistic values are reported with an accuracy of 1 cm s^{-1}.

Mooring	M11	M12	M13	M22a	M23a	M24a	M22b	M23b	M24b	M31	M32	M33	M34
Depth (m)	300	760	1042	1016	1315	1720	1560	1865	2270	500	976	1486	2100
Days	552	528	554	31	31	31	520	520	520	390	390	390	390
V_{max}	61	47	39	33	23	24	35	52	43	46	37	30	19
V	37	28	16	24	16	9	11	4	1	20	15	12	8
ϴ	0	0	3	-5	6	0	14	31	-23	-1	-1	5	7
u	0	0	-1	-2	2	0	3	2	0	0	0	1	1
σu	3	4	3	3	3	5	4	7	10	5	4	4	3
v	37	27	16	24	16	9	10	4	0	20	15	12	8
σv	10	7	7	5	5	7	4	3	5	7	6	6	5

919 **Table 3.** Statistics of ADCP observations at the oceanographic buoy between May 16 and June 7,
920 2016 (see location in Figure 1 and Table 1). C*i* denotes ADCP measurements, *i* denotes the level
921 measured from the surface. Here, **Θ** is the mean velocity direction (relative to the geographical
922 north), **V** (cm s^{-1}) is the magnitude of the time-average velocity and **v** (cm s^{-1}) and **u** (cm s^{-1}) are
923 the velocity components, **σ** is the standard deviation and unless otherwise specified, mean values
924 are indicated.
925

Mooring	Depth (m)	V_{max}	V	Θ	u	σu	v	σv
C1	10	66	54	0	-1	6	51	7
C2	20	71	55	-1	-1	5	53	8
C3	30	70	55	-1	-1	5	52	8
C4	40	68	53	-1	-1	4	51	8
C5	50	70	54	-2	-2	4	51	8
C6	60	70	56	-3	-4	6	53	8
C7	70	66	51	0	0	4	48	7
C8	80	64	48	-2	-2	4	46	7
C9	90	61	43	-3	-2	4	40	7
C10	100	61	46	-2	-2	3	44	7
C11	110	60	46	-1	-1	3	44	7
C12	120	59	45	-1	-1	3	43	7
C13	130	57	44	-1	-1	3	42	7
C14	140	55	41	-1	-1	3	39	6
C15	150	57	41	-25	0	4	39	7
C16	160	57	40	23	1	4	38	6
C17	170	55	39	1	1	4	36	6
C18	180	55	38	-2	1	4	35	7
C19	190	35	23	-41	2	3	21	5
C20	200	14	8	-15	-1	1	7	3

926

Table 4. Statistics of satellite derived velocities at the points closest to M1 and M3 (see locations in Figure 1 and Table 1). Here, **ϴ** is the mean velocity direction (relative to the true north), **V** (cm s^{-1}) is the magnitude of the time-average velocity, σ is the standard deviation and **v** (cm s^{-1}) and **u** (cm s^{-1}) are the velocity components.

	M1	**M3**
Days	552	390
V_{max} (cm s^{-1})	55	42
V (cm s^{-1})	44	26
ϴ	5	2
u (cm s^{-1})	4	1
σu (cm s^{-1})	2	4
v (cm s^{-1})	44	26
σv (cm s^{-1})	6	6

Supporting Information for

Malvinas Current at 44.7ºS: First assessment of velocity temporal variability from in situ data

Guillermina F. Paniagua[1,2,3], Martin Saraceno[1,2,3], Alberto R. Piola[2,3,5], Marcela Charo[5], Ramiro Ferrari[1,2,3], Camila Artana[6] and Christine Provost[4]

[1] Centro de Investigaciones del Mar y la Atmósfera (CIMA/CONICET-UBA), Ciudad Autónoma de Buenos Aires, Argentina

[2] Departamento de Ciencias de la Atmósfera y los Océanos, Facultad de Ciencias Exactas y Naturales, Universidad de Buenos Aires, Buenos Aires, Argentina

[3] Unidad Mixta Internacional-Instituto Franco-Argentino para el Estudio del Clima y sus Impactos (UMI-IFAECI/CNRS-CONICET-UBA), Buenos Aires, Argentina

[4] Laboratoire d'Océanographie et du Climat: Experimentation et Approches Numériques (LOCEAN), UMR 7159, Paris, Francia

[5] Departamento de Oceanografía, Servicio de Hidrografía Naval (SHN), Buenos Aires, Argentina

[6] MERCATOR OCEAN, Parc Technologique du Canal, Ramonville Saint Agne, France

Corresponding author: Guillermina F. Paniagua (guillermina.paniagua@cima.fcen.uba.ar)

Contents of this file

- Figures and their captions from S1 to S16:

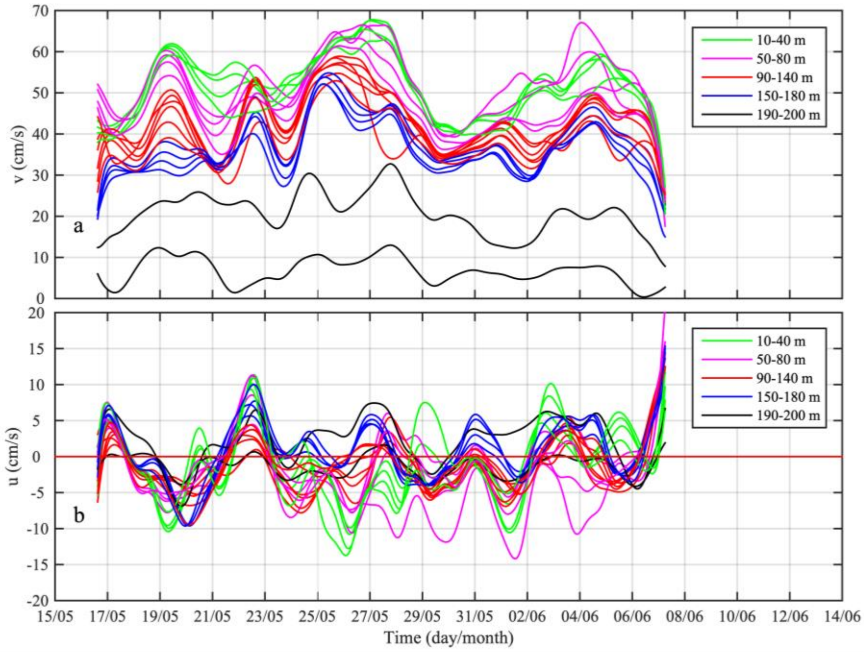

Figure S1. In situ time series of meridional (a) and zonal (b) velocities recorded by the oceanographic buoy at different depths.

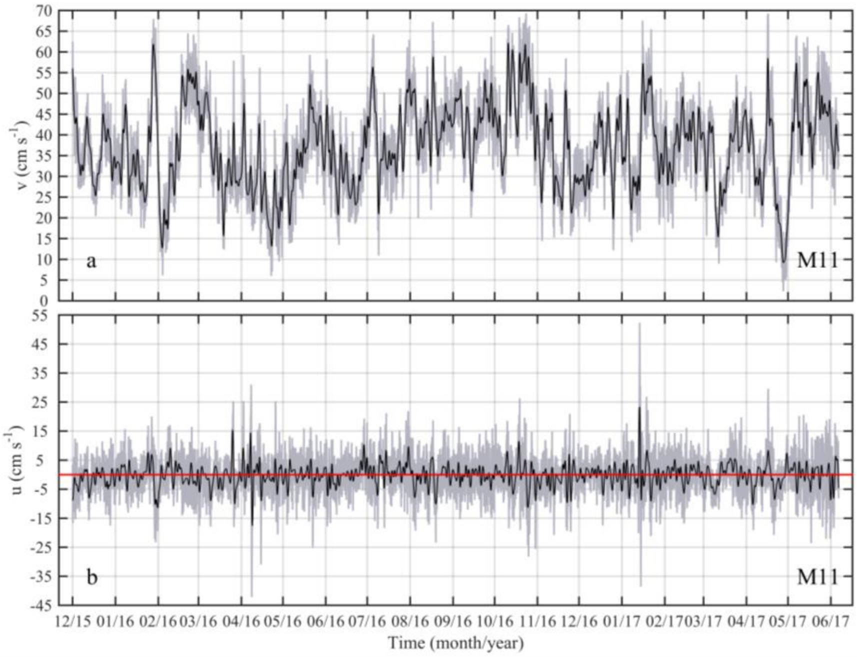

Figure S2. In situ time series of meridional (a) and zonal (b) velocities at M11 (mooring M1, 300 m). Light-gray lines correspond to raw data while black bold lines correspond to 48 h low-pass filtered data. Horizontal red lines correspond to the zero value. See Figure 2 for spatial location of the mooring.

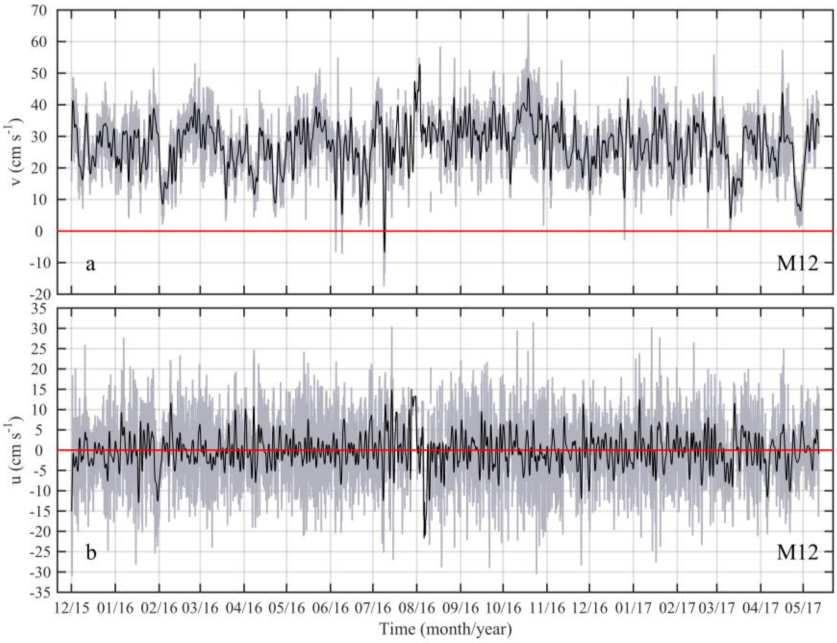

Figure S3. In situ time series of meridional (a) and zonal (b) velocities at M12 (mooring M1, 760 m). Light-gray lines correspond to raw data while black bold lines correspond to 48 h low-pass filtered data. Horizontal red lines correspond to the zero value. See Figure 2 for spatial location of the mooring.

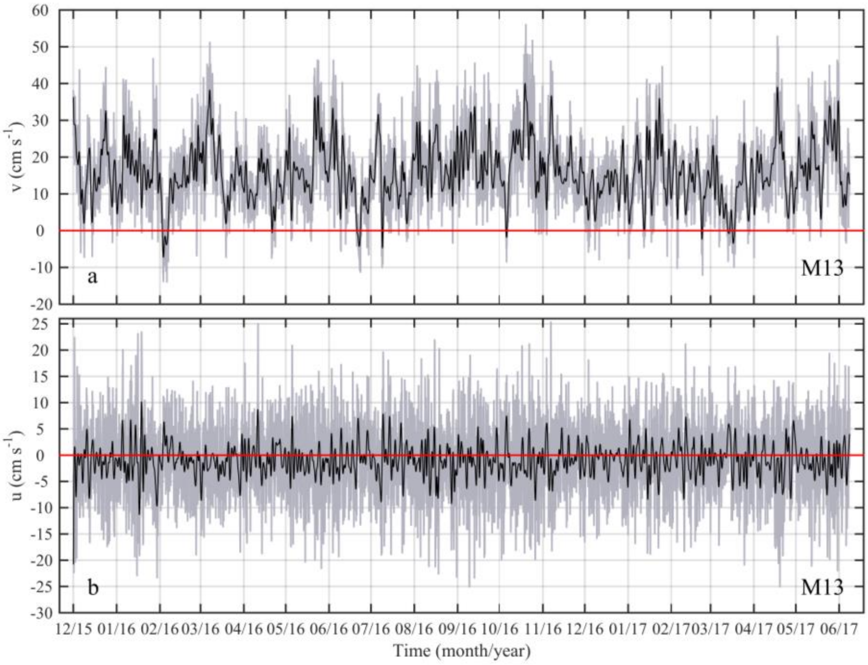

Figure S4. In situ time series of meridional (a) and zonal (b) velocities at M13 (instruments at 1042 m on mooring M1). Light-gray lines correspond to raw data while black bold lines correspond to 48 h low-pass filtered data. Horizontal red lines correspond to the zero value. See Figure 2 for spatial location of the mooring.

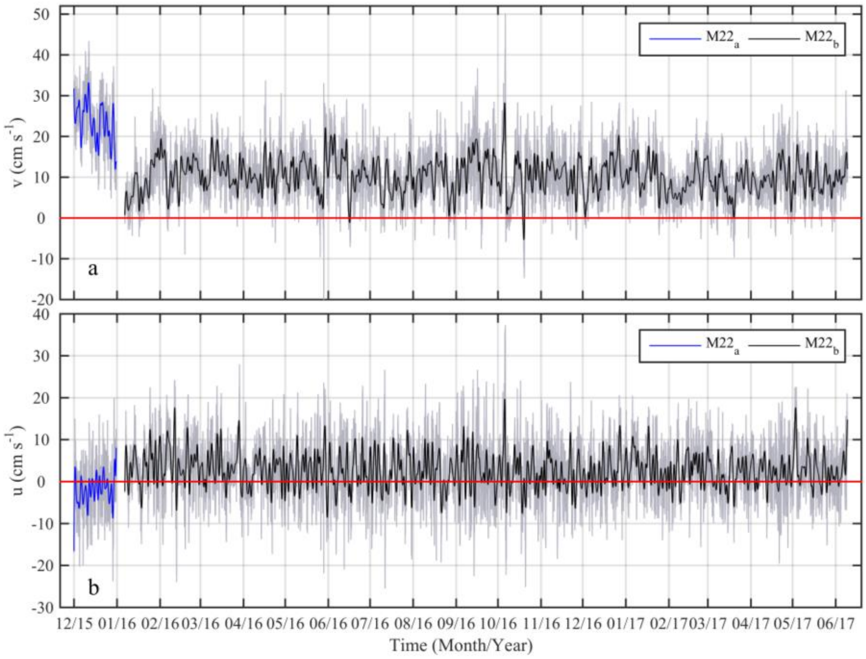

Figure S5. In situ time series of meridional (a) and zonal (b) velocities at M22a (instruments at 1016 m on mooring M2) and at M22b (instruments at 1560 m on mooring M2). Light-gray lines correspond to raw data while bold lines correspond to 48 h low-pass filtered data. Horizontal red lines correspond to the zero value. See Figure 2 for spatial location of the mooring.

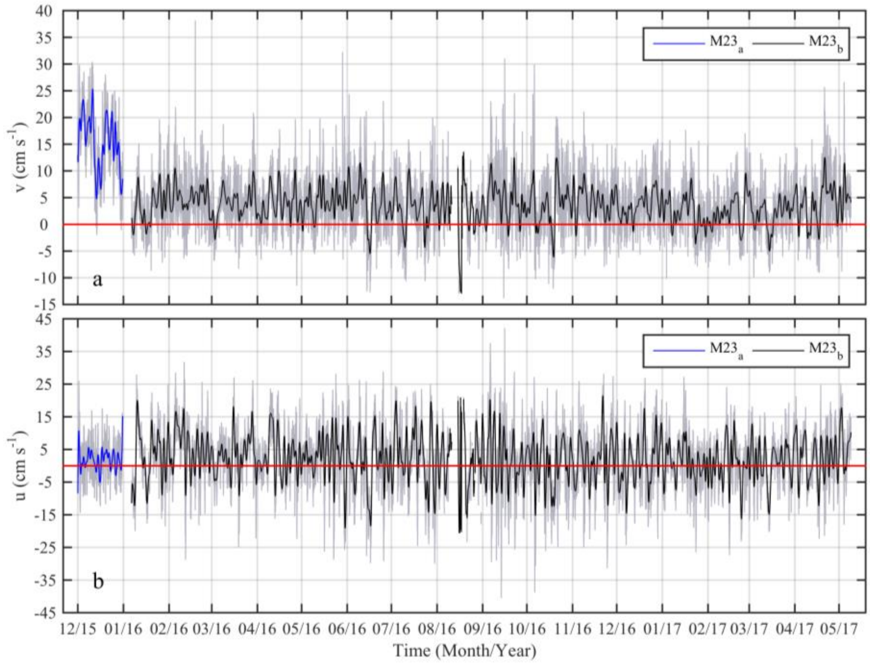

Figure S6. In situ time series of meridional (a) and zonal (b) velocities at M23a (instruments at 1315 m on mooring M2) and at M23b (instruments at 1865 m on mooring M2). Light-gray lines correspond to raw data while bold lines correspond to 48 h low-pass filtered data. Horizontal red lines correspond to the zero value. See Figure 2 for spatial location of the mooring.

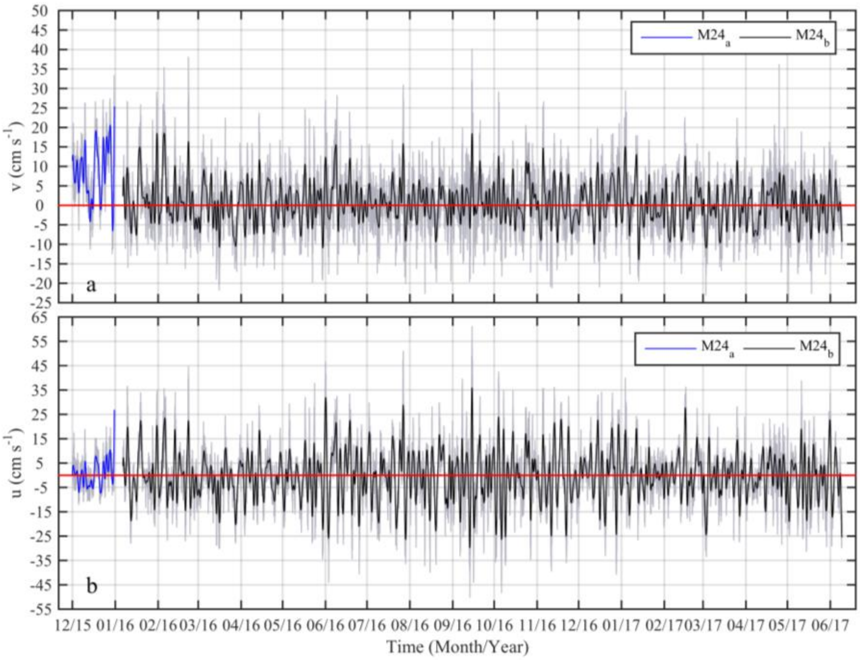

Figure S7. In situ time series of meridional (a) and zonal (b) velocities at M24a (instruments at 1720 m on mooring M2) and at M24b (instruments at 2270 m on mooring M2). Light-gray lines correspond to raw data while bold lines correspond to 48 h low-pass filtered data. Horizontal red lines correspond to the zero value. See Figure 2 for spatial location of the mooring.

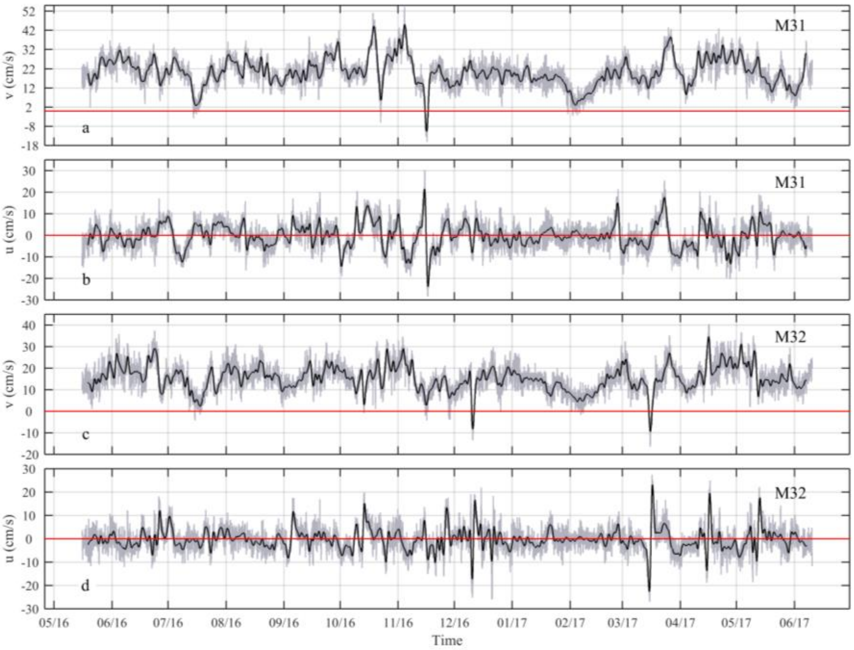

Figure S8. In situ time series of meridional (a) and zonal (b) velocities at M31 (mooring M3, 500 m) and at M32 (c and d; mooring M3, 976 m). Light-gray lines correspond to raw data while black bold lines correspond to 48 h low-pass filtered data. Horizontal red lines correspond to the zero value. See Figure 2 for spatial location of the mooring.

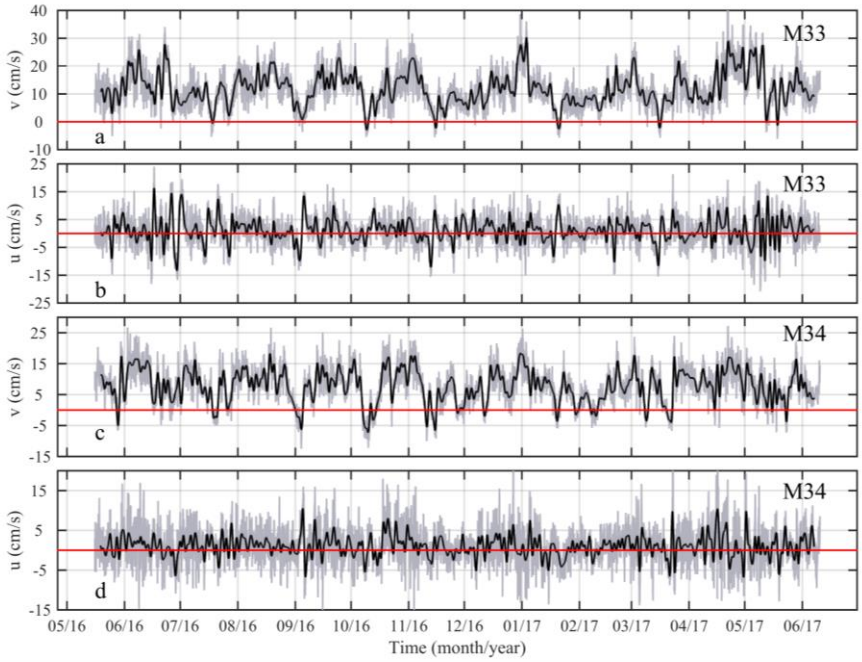

Figure S9. In situ time series meridional (a) and zonal (b) velocities at M33 (mooring M3, 1486 m) and at M34 (c and d; mooring M3, 2100 m). Light-gray lines correspond to raw data while black bold lines correspond to 48 h low-pass filtered data. Horizontal red lines correspond to the zero value. See Figure 2 for spatial location of the mooring.

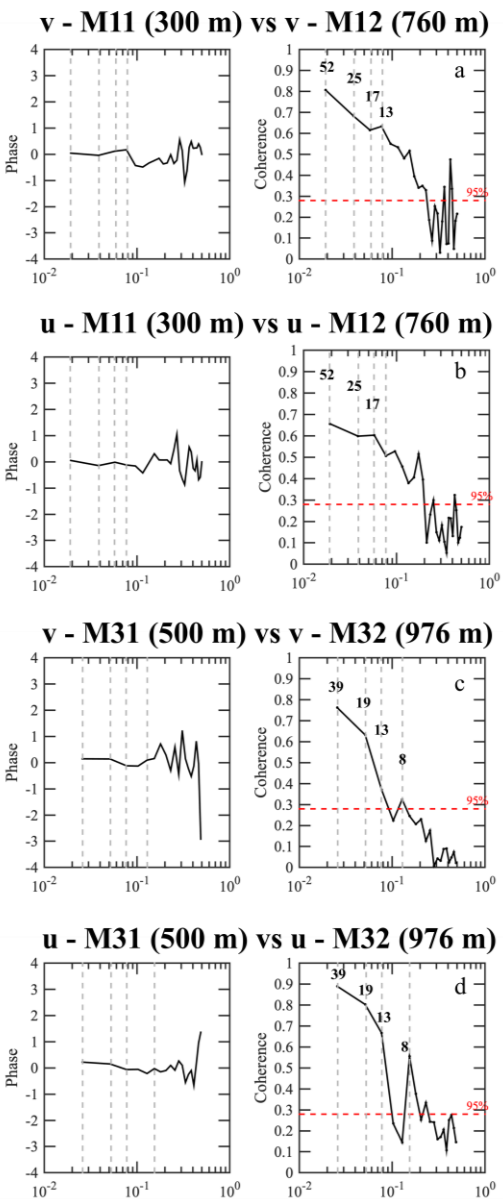

Figure S10. Coherence and phase lag spectra between the meridional and zonal velocities measured in the two uppermost current meters at M1 (a, b) and at M3 (c, d). The horizontal red dashed line in the coherence plots indicated the 95% confidence level.

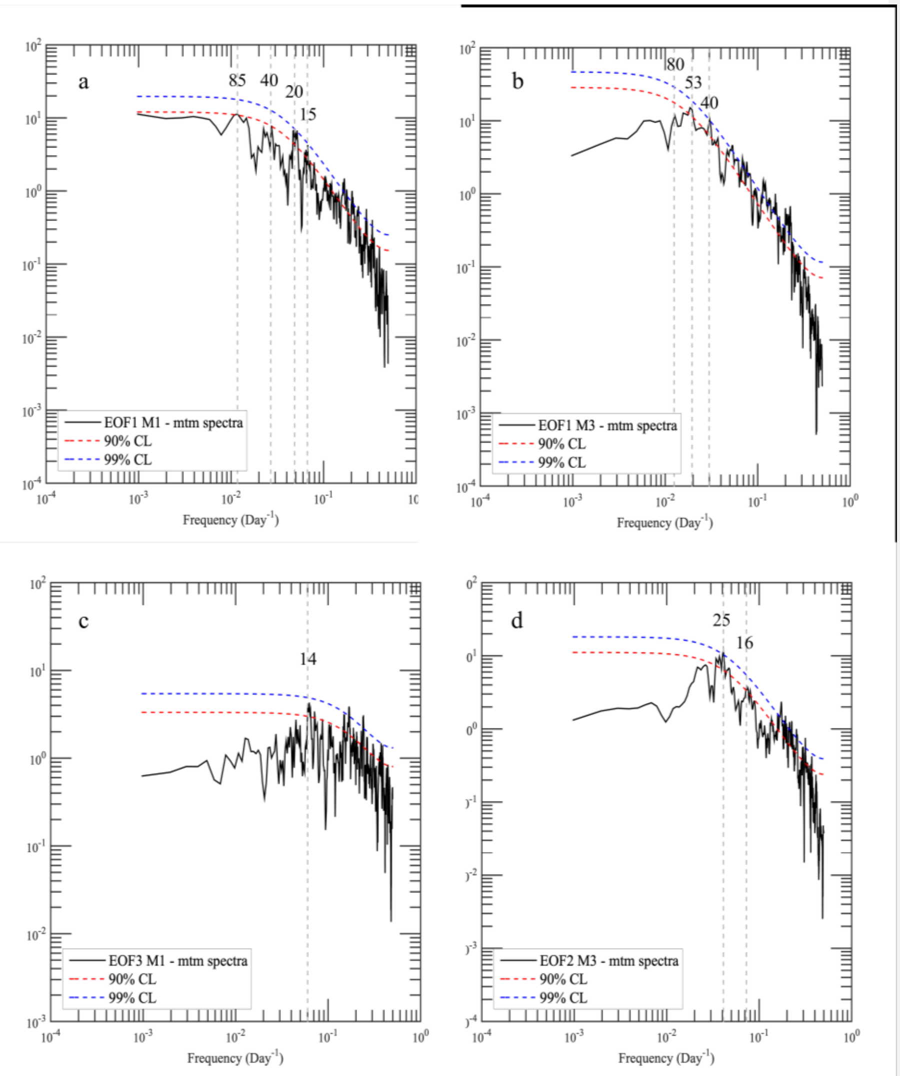

Figure S11. Spectra $(cm/s)^2/day^{-1}$ of the EOF1 of M1 (a), EOF1 of M3 (b), EOF3 of M1 (c) and EOF2 of M3 (d) time series. The logarithmic scale is applied on both axes. Vertical dashed lines and numbers indicate periodicities in days.

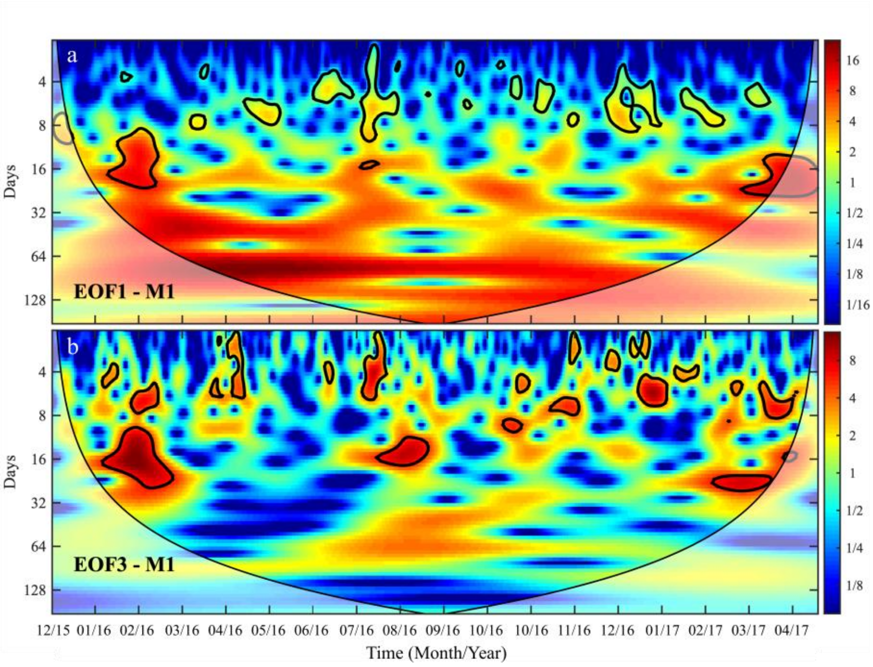

Figure S12. Wavelet power spectrum of (a) EOF1 and (b) EOF3 of M1 standardized time series. The thick black contour designates the 5% significance level against red noise and the cone of influence where edge effects might distort the picture is shown as lighter shade.

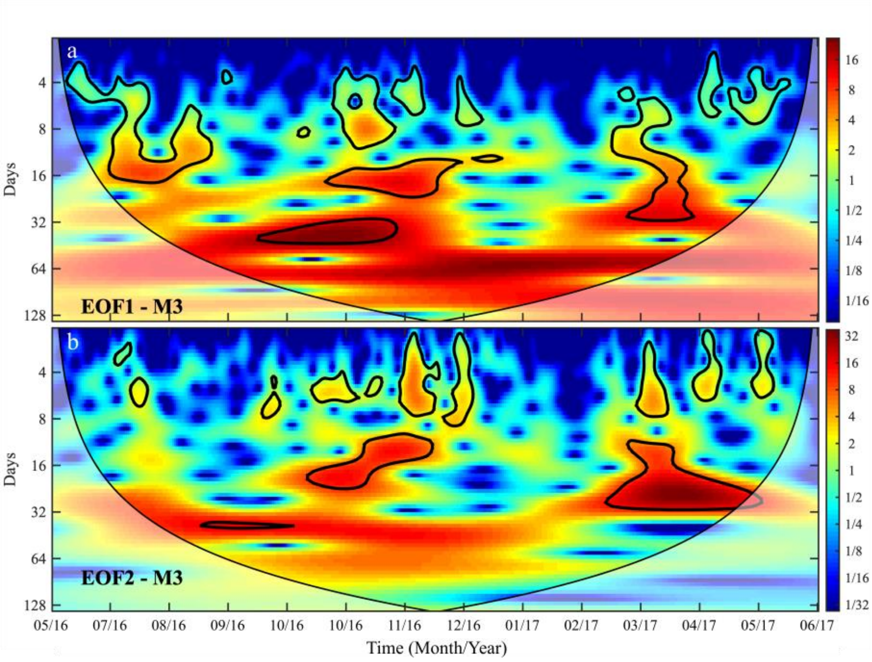

Figure S13. Wavelet power spectrum of (a) EOF1 and (b) EOF2 of M3 standardized time series. The thick black contour designates the 5% significance level against red noise and the cone of influence where edge effects might distort the picture is shown as lighter shade.

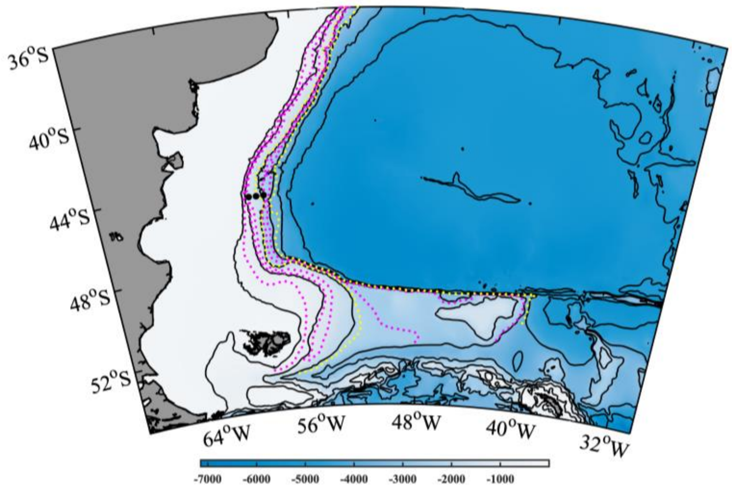

Figure S14. Dotted lines show the PV contours chosen to track the SLA variability. Magenta PV contours correspond from west to east with the following values: -20 10^{-8} m^{-1} s^{-1}, -10 10^{-8} m^{-1} s^{-1}, -8 10^{-8} m^{-1} s^{-1}, -4.6 10^{-8} m^{-1} s^{-1} and -4 10^{-8} m^{-1} s^{-1}. The yellow dotted lines denote the -3 10^{-8} m^{-1} s^{-1} and -5.2 10^{-8} m^{-1} s^{-1} PV contours, selected over the locations of maximum correlation between the along-slope velocities at M11 and M31 and the SLA across the MC at 44.7ºS. The black dots indicate the location of the mooring arrays.

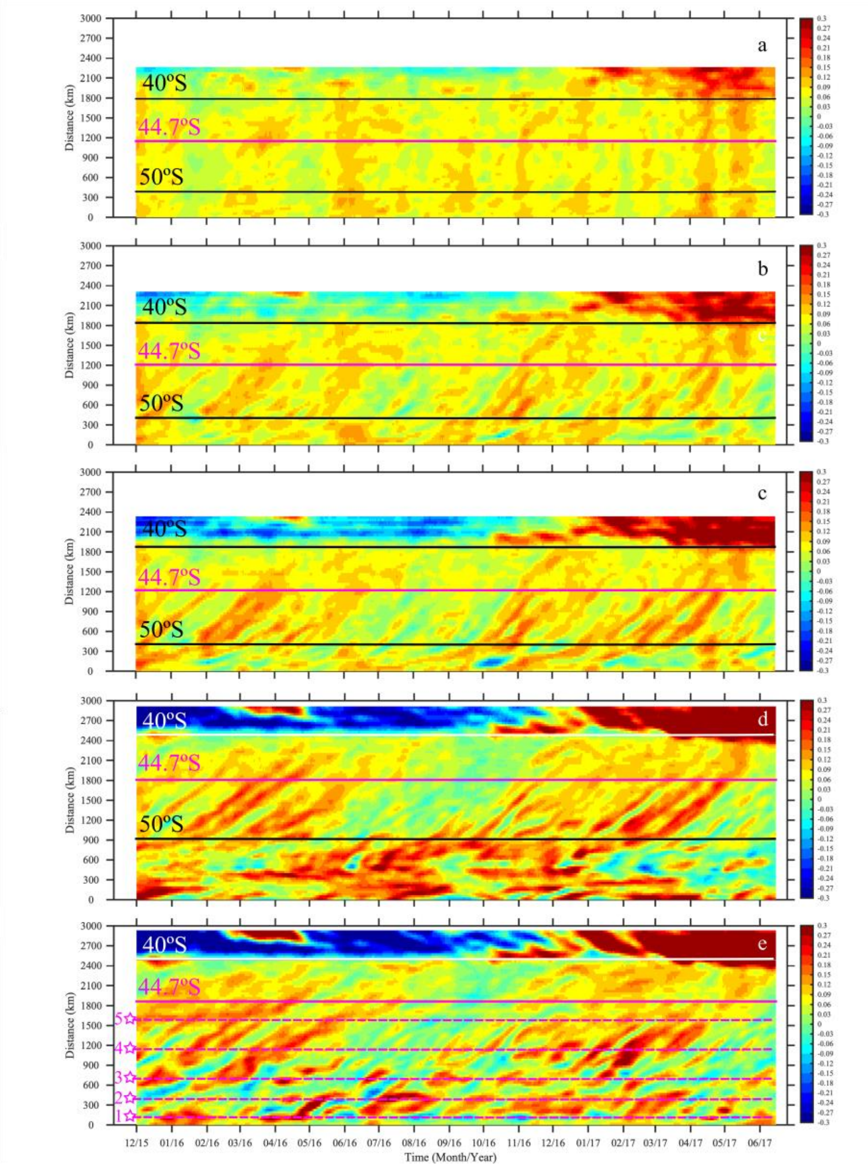

Figure S15. Distance vs time plot of SLA obtained over the following PV lines during CASSIS period: (a) -20 10^{-8} m^{-1} s^{-1}, (b) -10 10^{-8} m^{-1} s^{-1}, (c) -8 10^{-8} m^{-1} s^{-1}, (d) -4.6 10^{-8} m^{-1} s^{-1} and (e) -4 10^{-8} m^{-1} s^{-1}. The magenta line indicates the latitude of the mooring's location. The y-axis shows the distance from south to north (in km). The five magenta dashed lines mark the distances from "E1" indicated with stars in Figure 10a.

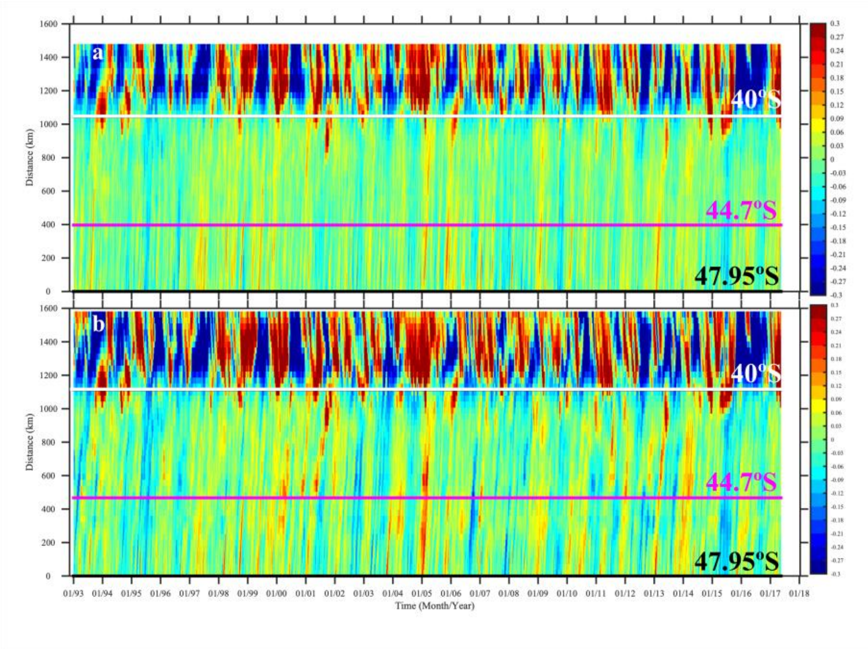

Figure S16. (a) Distance vs time plot of SLA obtained over the potential vorticity contour that goes from W1 to W2 from ~48ºS indicated in Figure 10a. The magenta line indicates the latitude of the mooring's location. The y-axis shows the distance from north to south (in km). (b) As in (a) but for the potential vorticity contour that goes from E1 to E2 in Figure 10a.

Formatted: English (United States)